CMS Physics Analysis Summary

Contact: cms-pag-conveners-top@cern.ch 2017/09/18

Measurement of differential cross sections for top quark pair production and associated jets using the lepton+jets final state in proton-proton collisions at 13 TeV

The CMS Collaboration

Abstract

Differential and double-differential cross sections for the production of top quark pairs in proton-proton collisions at 13 TeV are measured as a function of kinematic variables of the top quarks and the top quark-antiquark system. In addition, kinematic properties and multiplicities of jets associated with the production of top quark pairs are measured. This analysis is based on data collected by the CMS experiment at the LHC in 2016 corresponding to an integrated luminosity of 35.8 fb^{-1}. The measurements are performed in the lepton+jets decay channels with a single muon or electron and jets in the final state. The differential cross sections are presented at particle level, within a phase space close to the experimental acceptance, and at parton level in the full phase space. The results are compared to several standard model predictions that use different methods and approximations for their calculations. The kinematic properties of the top quarks and the top quark-antiquark system are well described apart from a softer transverse momentum of the top quarks, which has already been observed in previous measurements. The kinematic distributions and multiplicities of jets can be modeled by certain combinations of next-to-leading order calculations and parton shower models.

1 Introduction

Studies of the differential production cross sections of top quark pairs ($t\bar{t}$) at high energies yield crucial information for testing the standard model and searching for sources of new physics, which could alter the production rate. In particular, the differential $t\bar{t}$ cross sections probe predictions of quantum chromodynamics (QCD) and facilitate the comparisons of the data with state-of-the-art calculations. Some of the measured distributions, especially distributions of invariant mass and rapidity of the $t\bar{t}$ system, can be used to improve our understanding of parton distribution functions (PDFs). The measurement of kinematic properties and multiplicities of jets can provide insight into the tuning of the simulation of parton showers and hadronization.

Measurements of the $t\bar{t}$ differential and double-differential production cross sections as a function of kinematic variables of the top quarks and the $t\bar{t}$ system are presented. In addition, multiplicities and kinematic properties of jets in $t\bar{t}$ events are measured. The measurement is based on proton-proton (pp) collision data at a center-of-mass energy of 13 TeV corresponding to an integrated luminosity of $35.8\,\text{fb}^{-1}$ [1]. The data were recorded by the CMS experiment at the CERN LHC in 2016. Only $t\bar{t}$ decays into the ℓ+jets ($\ell = \text{e}, \mu$) final state are considered, where, after the decay of each top quark into a bottom quark and a W boson, one of the W bosons decays hadronically and the other one leptonically. Hence, the experimental signature consists of two jets coming from the hadronization of b quarks (b jets), two jets from a hadronically decaying W boson, a transverse momentum imbalance associated with the neutrino, and a single isolated muon or electron.

This measurement continues a series of differential $t\bar{t}$ production cross section measurements in pp collisions at the LHC. Previous measurements of differential cross sections at 7 TeV [2, 3] and 8 TeV [4–8] and of jet activities in $t\bar{t}$ events [9–12] have been performed in various $t\bar{t}$ decay channels. In addition, first measurements at 13 TeV are available [13, 14]. With about 15 times more data and an improved understanding of systematic uncertainties we provide an update and extension to the previous analysis in the ℓ+jets channel [15] at 13 TeV.

We measure differential cross sections defined in two different ways, at particle level and at parton level. For the particle-level measurement a proxy of the top quark is defined based on experimentally accessible quantities like jets, which consist of quasi-stable particles with a mean lifetime greater than 30 ps. These are described by theoretical predictions that require a modeling of the parton shower and hadronization, in addition to the matrix-element calculations. The kinematic selections of these objects are closely reproducing the experimental acceptance. Electrons and muons stemming from τ lepton decays are not treated separately and can contribute to the particle-level signal. A detailed definition of particle-level objects is given in Section 3. The particle-level approach has the advantage that it reduces theoretical uncertainties in the experimental results by avoiding theory-based extrapolations from the experimentally accessible portion of the phase space to the full range, and from jets to partons.

The parton-level top quarks in the ℓ+jets decay channel are extracted from the calculation directly before decaying into a bottom quark and a W boson. The τ+jets decay channel is not considered here as signal even if the event contains an electron or muon from a τ lepton decay. The $t\bar{t}$ production is calculated at next-to-leading order (NLO) and combined with a simulation of the parton shower. No restriction of the phase space is applied for parton-level top quarks.

At particle and parton level differential cross sections are measured as a function of the transverse momentum p_{T} and the absolute rapidity $|y|$ of the top quarks with the hadronically (t_{h}) and the leptonically (t_ℓ) decaying W boson; as a function of p_{T}, $|y|$, and mass M of the $t\bar{t}$ system. In addition, at parton level the differential cross sections as a function of the p_{T} of the top

quarks with the higher and lower p_T are measured. Double-differential cross sections for the following combinations of variables are determined at both levels: $|y(t_h)|$ *vs.* $p_T(t_h)$, $M(t\bar{t})$ *vs.* $|y(t\bar{t})|$, and $p_T(t_h)$ *vs.* $M(t\bar{t})$. At particle level differential cross sections as a function of $p_T(t_h)$, $p_T(t\bar{t})$, and $M(t\bar{t})$ are measured in bins of jet multiplicity. For the four jets identified as the $t\bar{t}$ decay products and the four leading additional jets the cross sections as function of jet p_T, $|\eta|$, the minimal separation ΔR_{jt} of jets from the jets in the $t\bar{t}$ system, and the separation ΔR_t of jets from the closer top quark are measured, where the cone $\Delta R = \sqrt{(\Delta\phi)^2 + (\Delta\eta)^2}$. Finally, we determine the gap fraction, defined as the fraction of events that do not contain jets above a given p_T threshold, and jet multiplicities for various thresholds of the jet p_T.

2 Signal and background modeling

The Monte Carlo generators POWHEG [16–19] (v2) and MADGRAPH5_aMC@NLO [20] (v2.2.2) (MG5_aMC@NLO) are used to simulate $t\bar{t}$ events. They include NLO QCD matrix element calculations that are combined with the parton-shower simulation of PYTHIA8 [21, 22] (v8.205) using the tune CUETP8M2T4 [23]. In addition, MG5_aMC@NLO is used to produce a simulation of $t\bar{t}$ events with additional partons. All processes of up to two additional partons are calculated at NLO and combined with the PYTHIA8 parton-shower simulation using the FxFx [24] algorithm. The default parametrization of the PDFs used in all simulations is NNPDF30_nlo_as_0118 [25]. A top quark mass $m_t = 172.5\,\text{GeV}$ is used. The simulations are normalized to an inclusive $t\bar{t}$ production cross section of $832^{+40}_{-46}\,\text{pb}$ [26]. This value is calculated with next-to-NLO (NNLO) precision including the resummation of next-to-next-to-leading-logarithmic (NNLL) soft gluon terms. Its uncertainty is evaluated regarding the choice of renormalization/factorization scales and PDFs.

In all simulations, event weights are calculated that represent the usage of the uncertainty eigenvector sets of the PDFs. There are also event weights available that represent the changes of factorization and renormalization scales by a factor of two or one half. These additional weights allow for the calculation of systematic uncertainties due to the PDFs and the scale choices. For additional uncertainty estimations we use POWHEG+PYTHIA8 simulations with top quark masses of 171.5 and 173.5 GeV, with initial and final parton-shower scales varied up and down by a factor of two, variations of the underlying event tune, and a simulation with activated color reconnection of resonant decays. For further comparison, a simulation with POWHEG combined with HERWIG++ [27] (v2.7.1) using the EE5C tune [28] is used.

The main backgrounds are produced using the same techniques. The MG5_aMC@NLO generator is used for the simulation of W boson production in association with jets, *t*-channel single top quark production, and Drell–Yan (DY) production in association with jets. The POWHEG [29] generator is used for the simulation of single top quark associated production with a W boson (tW) and PYTHIA8 is used for multijet production. In all cases the parton shower and the hadronization are described by PYTHIA8. The W boson and DY backgrounds are normalized to their NNLO cross sections [30]. The single top quark processes are normalized to NLO calculations [31, 32], and the multijet simulation is normalized to the LO calculation [22].

The detector response is simulated using GEANT4 [33]. Finally, the same reconstruction algorithms that are applied to the data are used. The simulations include multiple pp interactions per bunch crossing (pileup). Their multiplicity is in agreement with that observed during the data taking.

3 Particle-level top quark definition

The definitions of objects constructed from quasi-stable particles, obtained from the predictions of $\mathrm{t\bar{t}}$ event generators before any detector simulation, is summarized below. These objects are further used to define the particle-level top quarks. Detailed studies on particle-level definitions can be found in [34].

- All muons and electrons are corrected for final-state radiation by adding the photon momenta to the momentum of the closest lepton if their separation is $\Delta R < 0.1$. All photons are considered for the momentum correction. A corrected lepton is selected if it fulfills the isolation requirement that the p_T sum of all quasi-stable particles, excluding corrected leptons and neutrinos, within $\Delta R = 0.4$ is less than 35% of the corrected lepton p_T. In addition, we require $p_\mathrm{T} > 15\,\mathrm{GeV}$ and $|\eta| < 2.4$.
- Photons with $p_\mathrm{T} > 15\,\mathrm{GeV}$ and $|\eta| < 2.4$ that are not used in the momentum correction of a lepton are considered. Their isolation is defined in the same way as for electron and muons. However, they are selected as isolated photons if the isolation is below 25%.
- All neutrinos are selected.
- Jets are clustered by the anti-k_T jet algorithm [35, 36] with a distance parameter of 0.4. All quasi-stable particles with the exception of neutrinos are clustered. Jets with $p_\mathrm{T} > 25\,\mathrm{GeV}$ and $|\eta| < 2.4$ are selected if there is no isolated lepton or photon, as selected above, within a $\Delta R = 0.4$.
- b jets at particle level are defined as those jets that contain a b hadron. As a result of the short lifetime of b hadrons, only their decay products should be considered for the jet clustering. However, to allow their association to a jet, the b hadrons are also included with their momenta scaled down to a negligible value. This preserves the information of their directions, but they have no impact on the jet clustering itself.

Based on the invariant masses M of these objects, we construct a pair of particle-level top quarks in the ℓ+jets final state. Events with exactly one muon or electron with $p_\mathrm{T} > 30\,\mathrm{GeV}$ and $|\eta| < 2.4$ are selected. Events with an additional muon or electron with $p_\mathrm{T} > 15\,\mathrm{GeV}$ and $|\eta| < 2.4$ are rejected. We take the sum of the four-momenta of all neutrinos as the neutrino momentum p_ν from the leptonically decaying top quark and find the permutation of jets that minimizes the quantity

$$K^2 = [M(p_\nu + p_\ell + p_{\mathrm{b}_\ell}) - m_\mathrm{t}]^2 + [M(p_{\mathrm{jW1}} + p_{\mathrm{jW2}}) - m_\mathrm{W}]^2 + [M(p_{\mathrm{jW1}} + p_{\mathrm{jW2}} + p_{\mathrm{b}_\mathrm{h}}) - m_\mathrm{t}]^2, \quad (1)$$

where $p_{\mathrm{jW1/2}}$ are the four-momenta of two light-flavor jet candidates, considered as the decay products of the hadronically decaying W boson, $p_{\mathrm{b}_{\ell/\mathrm{h}}}$ are the four-momenta of two b-jet candidates, p_ℓ is the four-momentum of the lepton, and $m_\mathrm{W} = 80.4\,\mathrm{GeV}$ is the mass of the W boson. All jets with $p_\mathrm{T} > 25\,\mathrm{GeV}$ and $|\eta| < 2.4$ are considered. At least four jets are required, of which at least two must be b jets. The remaining jets with $p_\mathrm{T} > 30\,\mathrm{GeV}$ and $|\eta| < 2.4$ are defined as additional jets.

It should be remarked that events with a hadronically and a leptonically decaying particle-level top quark are not required to be ℓ+jets events at the parton level, e.g., $\mathrm{t\bar{t}}$ dilepton events with additional jets can be identified as ℓ+jets event at particle level if one lepton fails to pass the selection. As an example, in Fig. 1 the relation between the $p_\mathrm{T}(\mathrm{t_h})$ values at particle and parton level is shown.

To obtain an unambiguous nomenclature of the jets we define j_{W1} to be the jet in the W boson decay with the higher p_T. The additional jets j_i are sorted by their transverse momenta where j_1 has the highest p_T.

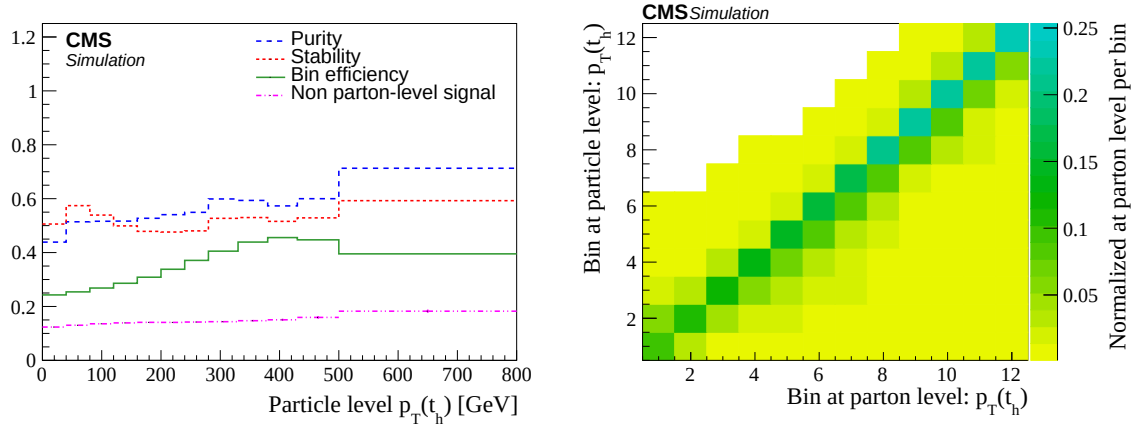

Figure 1: Comparison between the $p_T(t_h)$ at particle and parton level, extracted from the POWHEG+PYTHIA8 simulation. Left: fraction of parton-level top quarks in the same bin at particle level (purity), fraction of particle-level top quarks in the same bin at parton level (stability), ratio of the number of particle- to parton-level top quarks, and fraction of events with a particle-level top quark pair that are not considered as signal events at parton level. Right: bin migrations between particle and parton level. The p_T range of the bins can be taken from the left panel. Each column is normalized to the number of events per column at parton level in the full phase space.

4 Physics object reconstruction

This analysis depends on the reconstruction and identification of muons, electrons, jets, and missing transverse momentum associated with a neutrino. Only leptons are selected that are compatible with originating from the primary vertex where the reconstructed vertex with the largest value of summed physics-object p_T^2 is taken to be the primary pp interaction vertex. The physics objects are the objects returned by a jet finding algorithm [35, 36] applied to all charged tracks associated with the vertex, plus the corresponding associated missing transverse momentum. Leptons from $t\bar{t}$ decays are typically isolated. Hence a requirement on the lepton isolation is used to reject leptons produced in decays of hadrons.

The muon isolation variable is defined as the sum of the p_T of neutral hadrons, charged hadrons, and photon PF candidates within a cone of $\Delta R = 0.4$. It is required to be less than 15% of the muon p_T. The muon reconstruction and selection [37] efficiency is measured in the data using tag-and-probe techniques. Depending on the p_T and η of the muon it is 75–85%.

For electrons the isolation variable is the sum of the p_T of neutral hadrons, charged hadrons, and photon PF candidates in a cone of $\Delta R = 0.3$ around the electron. This isolation variable is required to be smaller than 6% of the electron p_T. An event-by-event correction is applied that maintains a constant electron isolation efficiency with respect to the number of pileup interactions [38]. The measured reconstruction and identification [39] efficiency for electrons is 50–80% with a p_T and η dependence.

Jets are reconstructed from PF objects clustered using the anti-k_T jet algorithm with a distance parameter of 0.4 using the FASTJET package [36]. Charged particles originating from a vertex of a pileup interaction are excluded. The total energy of the jets is corrected for energy depositions

from pileup. In addition, p_T- and η-dependent corrections are applied to correct for detector response effects [40]. Those jets identified as isolated muons or electrons are removed from consideration.

For the identification of b jets the combined secondary vertex algorithm [41] is used. It provides a discriminant between light-flavor and b jets based on the combined information of secondary vertices and the impact parameter of tracks at the primary vertex. A jet is identified as b jet if the associated value of the discriminant exceeds a threshold criterion with an efficiency of about 63% and a combined charm and light-flavor jet rejection probability of 97%.

The missing transverse momentum $\vec{p}_T^{\,miss}$ is calculated as the negative of the vectorial sum of transverse momenta of all PF candidates in the event. Jet energy corrections are also propagated to improve the measurement of $\vec{p}_T^{\,miss}$.

5 Event selection

Events are selected if they pass single-lepton triggers. These require $p_T > 27\,GeV$ for electrons and $p_T > 24\,GeV$ for muons, as well as various quality and isolation criteria.

To reduce the background contributions and optimize the $t\bar{t}$ reconstruction additional, more stringent, requirements on the events are imposed. Events with exactly one muon or electron with $p_T > 30\,GeV$ and $|\eta| < 2.4$ are selected. No additional muons or electrons with $p_T > 15\,GeV$ and $|\eta| < 2.4$ are allowed. In addition to the lepton, at least four jets with $p_T > 30\,GeV$ and $|\eta| < 2.4$ are required. At least two of these jets must be tagged as b jets.

We compare several kinematic distributions of the muon and electron channels to the simulation to verify that there are no unexpected differences. The ratios of the measured to the expected event yields in the two channels agree within the uncertainty in the lepton reconstruction and selection efficiencies. In the remaining steps of the analysis the two channels are combined by adding their distributions.

6 Reconstruction of the top quark-antiquark system

The goal of the $t\bar{t}$ reconstruction is the correct identification of reconstructed objects as parton- or particle-level top quark decay products. To test the performance of the reconstruction algorithm an assignment between detector level and parton- (particle-) level objects is needed. For the particle-level measurement this relationship is straightforward. Reconstructed leptons and jets can be matched spatially to corresponding objects at the particle level. For the parton-level measurement we need to define how to match the four initial quarks from a $t\bar{t}$ decay with reconstructed jets. This is not free of ambiguities since a quark does generally not lead to a single jet. One quark might shower into several jets or multiple quarks might be clustered into one jet if they are not well separated. We introduce an unambiguous matching criterion that matches the reconstructed jet with the highest p_T within $\Delta R = 0.4$ to a quark from the $t\bar{t}$ decay. If two quarks are matched with the same jet, the event has a merged topology and is considered as "not reconstructible" in the context of this analysis.

For the reconstruction of the top quark-antiquark system all possible permutations of jets that assign reconstructed jets to the decay products of the $t\bar{t}$ system are tested and a likelihood that a certain permutation is correct is evaluated. Permutations are considered only if the two jets with the highest b identification probabilities are the two b-jet candidates. In each event the permutation with the highest likelihood is selected. The likelihoods are evaluated separately

for the particle- and the parton-level measurements.

The first reconstruction step involves the determination of the neutrino four-momentum p_ν. This is performed using the algorithm described in Ref. [42]. The idea is to find all possible solutions for the three components of the neutrino momentum using the two mass constraints $(p_\nu + p_\ell)^2 = m_{\mathrm{W}}^2$ and $(p_\nu + p_\ell + p_{\mathrm{b}_\ell})^2 = m_{\mathrm{t}}^2$. Each equation describes an ellipsoid in the three-dimensional momentum space of the neutrino. The intersection of these two ellipsoids is usually an ellipse. We select p_ν as the point on the ellipse for which the distance $D_{\nu,\mathrm{min}}$ between the ellipse projection onto the transverse plane and $\vec{p}_{\mathrm{T}}^{\,\mathrm{miss}}$ is minimal. This algorithm leads to a unique solution for the longitudinal neutrino momentum and an improved resolution for the transverse component. The minimum distance $D_{\nu,\mathrm{min}}$ can also be used to identify the correct b_ℓ. In the cases with an invariant mass of the lepton and the b_ℓ candidate above m_{t} no solution can be found and we continue with the next permutation.

The likelihood λ is maximized to select the best permutation of jets. It uses constraints of the top quark and W boson masses on the hadronic side and the $D_{\nu,\mathrm{min}}$ value from the neutrino reconstruction, and is defined by

$$-\log(\lambda) = -\log(P_m(m_2, m_3)) - \log(P_\nu(D_{\nu,\mathrm{min}})), \tag{2}$$

where P_m is the two-dimensional probability density of the invariant masses of W bosons and top quarks, which are correctly reconstructed based on the matching criteria described above. This probability is calculated as a function of the invariant mass of the two jets m_2 tested as the W boson decay products, and the invariant mass of the three jets m_3 tested as the decay products of the hadronically decaying top quark. The distributions for the correct jet assignments, taken from the POWHEG+PYTHIA8 simulation and normalized to unity, are shown in Fig. 2 for the particle- and parton-level measurements. This part of the likelihood is sensitive to the correct reconstruction of the hadronically decaying top quark. Permutations with probabilities of less than 0.1% of the maximum value of the probability density P_m are rejected. Especially in the parton-level measurement this selection criterion removes events that are incompatible with the hypothesis of a hadronically decaying top quark and reduces the background contribution.

The probability density P_ν describes the distribution of $D_{\nu,\mathrm{min}}$ for a correctly selected b_ℓ. In Fig. 2 the normalized distributions of $D_{\nu,\mathrm{min}}$ for b_ℓ and for other jets are shown. On average, the distance $D_{\nu,\mathrm{min}}$ for correctly selected b_ℓ is smaller and has a lower tail compared to the distance obtained for other jets. Permutations with values of $D_{\nu,\mathrm{min}} > 150\,\mathrm{GeV}$ are rejected since they are very unlikely to originate from a correct b_ℓ association. This part of the likelihood is sensitive to the correct reconstruction of the leptonically decaying top quark.

The likelihood λ combines the probabilities from the reconstruction of the hadronically and leptonically decaying top quarks and provides information on reconstructing the whole $\mathrm{t\bar{t}}$ system. The performance of the reconstruction algorithm is tested using the three $\mathrm{t\bar{t}}$ simulations generated with POWHEG combined with PYTHIA8 or HERWIG++, and MG5_aMC@NLO+PYTHIA8 where we use the input distributions P_m and P_ν from POWHEG+PYTHIA8. The reconstruction efficiency of the algorithm is defined as the probability that the most likely permutation, as identified through the maximization of the likelihood λ, is the correct one, given that all decay products from the $\mathrm{t\bar{t}}$ decay are reconstructed and selected. These efficiencies as a function of the jet multiplicity are shown in Fig. 3. Since the number of permutations increases drastically with the number of jets, it is more likely to select a wrong permutation if there are additional jets. The small differences observed in different simulations are taken into account for

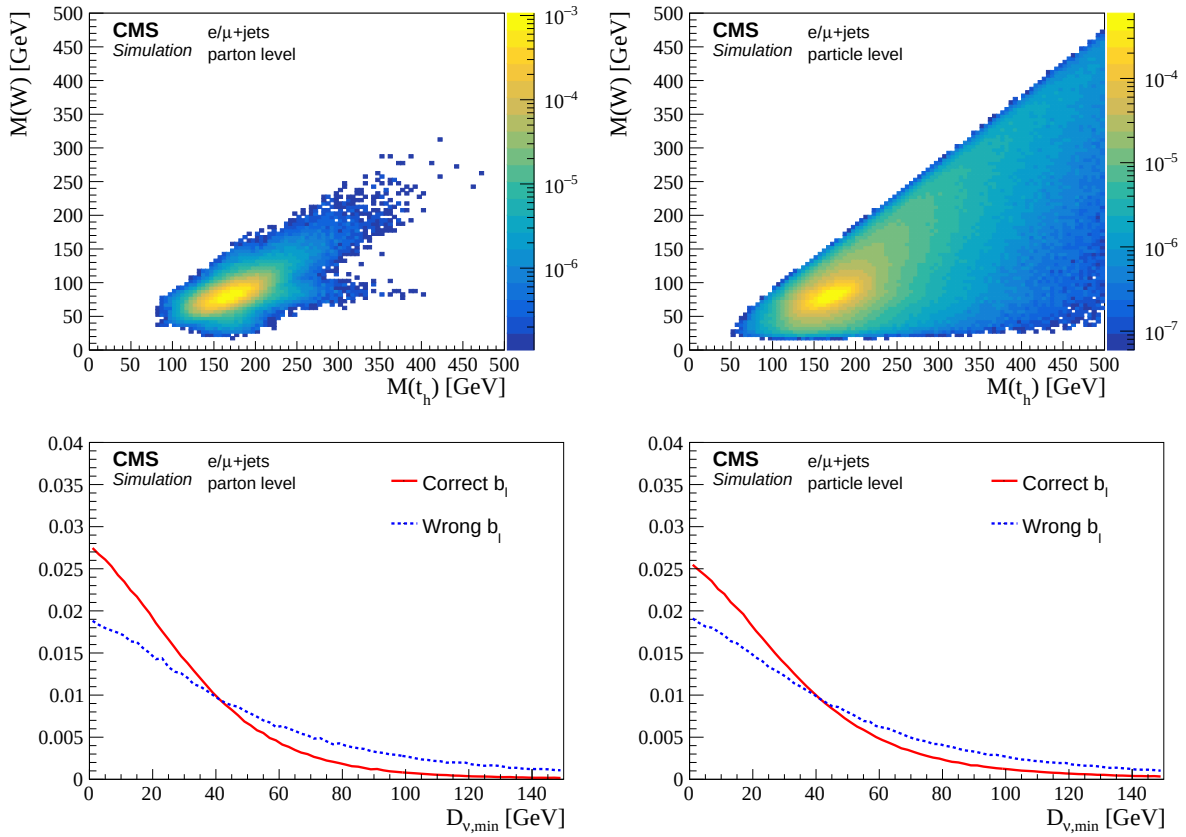

Figure 2: Top: normalized two-dimensional mass distribution of the correctly reconstructed hadronically decaying W bosons $M(\mathrm{W})$ and the correctly reconstructed top quarks $M(\mathrm{t_h})$ for the parton- (left) and the particle- (right) level measurements. The predictions of the other contributions are taken from the simulation. Bottom: normalized distributions of the distance $D_{\nu,\mathrm{min}}$ for correctly and wrongly selected b jets from the leptonically decaying top quarks. The distributions are taken from the POWHEG+PYTHIA8 $\mathrm{t\bar{t}}$ simulation.

the uncertainty estimations. We observe a lower reconstruction efficiency for the particle-level measurement. This is caused by the weaker mass constraints for a particle-level top quark, where, in contrast to the parton-level top quark, exact matches to the top quark and W boson masses are not required. This can be seen in the mass distributions of Fig. 2 and the likelihood distributions in Fig. 4. Here the signal simulation is divided into the following categories: correctly reconstructed $\mathrm{t\bar{t}}$ systems ($\mathrm{t\bar{t}}$ right reco), events where all decay products are available, but the algorithm failed to identify the correct permutation ($\mathrm{t\bar{t}}$ wrong reco), ℓ+jets $\mathrm{t\bar{t}}$ events where at least one decay product is missing ($\mathrm{t\bar{t}}$ not reconstructible), and nonsignal $\mathrm{t\bar{t}}$ events ($\mathrm{t\bar{t}}$ nonsignal). However, the lower reconstruction efficiency of the particle-level top quark is compensated by the higher number of reconstructible events.

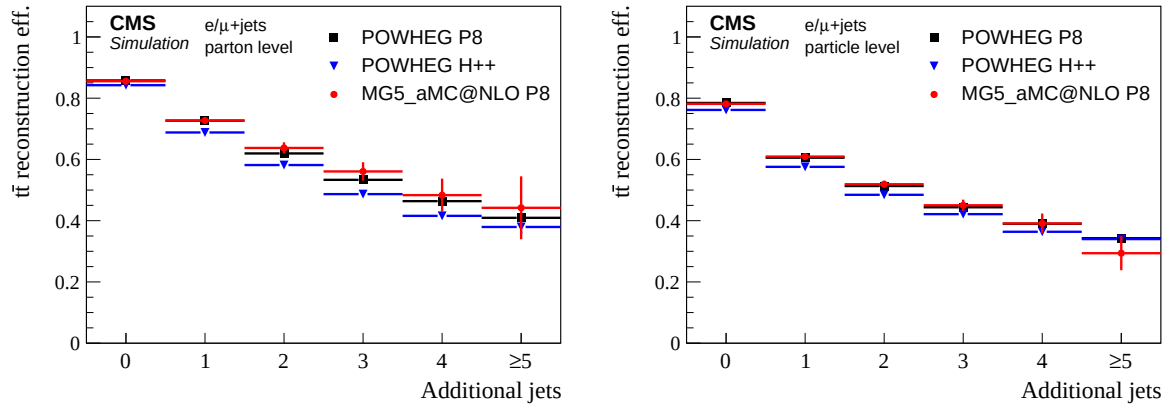

Figure 3: Reconstruction efficiency of the $\mathrm{t\bar{t}}$ system as a function of the number of additional jets for the parton- (left) and particle- (right) level measurements. The efficiencies are calculated based on the simulations with POWHEG+PYTHIA8 (P8), POWHEG+HERWIG++ (H++), and MG5_aMC@NLO +PYTHIA8. The efficiencies are shown with statistical uncertainties depending on the simulation.

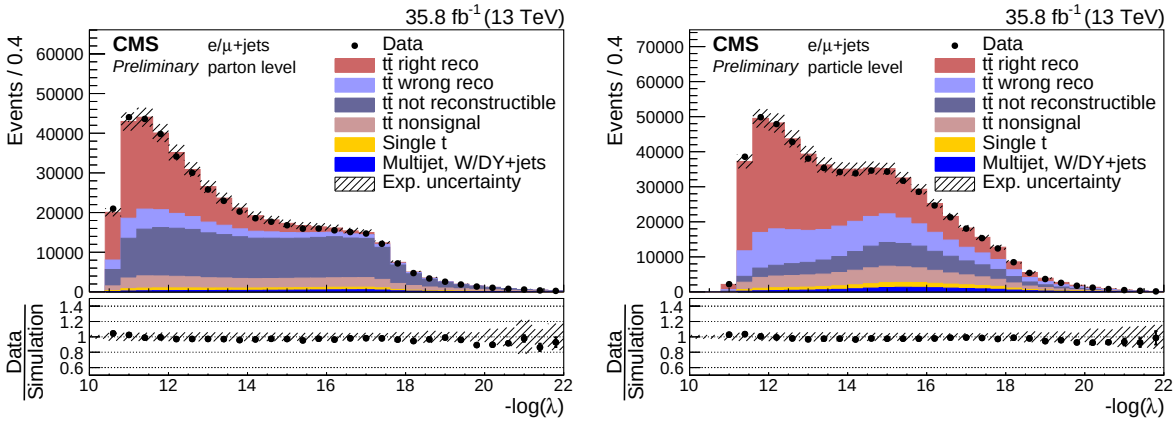

Figure 4: Distribution of the negative log-likelihood for the selected best permutation in the parton- (left) and the particle- (right) level measurements in data and simulations. The simulation of POWHEG+PYTHIA8 is used to describe the $\mathrm{t\bar{t}}$ production. The contribution of multijet, DY, and W boson events is extracted from the data (cf. Section 7). Experimental (cf. Section 9) and statistical uncertainties (hatched area) are shown for the total simulated yield, which is normalized to the measured integrated luminosity of the data. The data points are shown with statistical uncertainties. The ratios of data to the sum of the expected yields are provided at the bottom of each panel.

In Fig. 5 the p_T of the jets of the $t\bar{t}$ system, as identified by the reconstruction algorithm, and of the additional jets are presented and compared to the simulation. In Fig. 6 the distributions of p_T and $|y|$ of the reconstructed top quarks and in Fig. 7 the distributions of $p_T(t\bar{t})$, $|y(t\bar{t})|$, and $M(t\bar{t})$ for the parton- and particle-level measurements are shown. In general, good agreement is observed between the data and the simulation though the measured p_T spectra of the top quarks and of additional jets are softer than expected.

7 Background subtraction

After the event selection and the parton- (particle-) level $t\bar{t}$ reconstruction about 450 000 (570 000) events are observed. A small contribution of about 4.5% (6.0%) of single top quark, DY, W boson, and multijet events is expected. These have to be estimated and subtracted from the selected data. In addition, a residual contamination from nonsignal $t\bar{t}$ events is expected and estimated from the simulation as detailed below.

The background from single top quark production is subtracted based on its simulation. Its overall contribution corresponds to about 2.7% (3.3%) of the selected data in the parton- (particle-) level measurements. Single top quark production cross sections are calculated with precisions of a few percent [31, 32]. Since the calculations have a limited reliability after $t\bar{t}$ selection we assume an overall uncertainty of 50%. However, this conservative estimate has negligible impact on the final results and their accuracy.

The simulations of multijet, DY, and W boson production contain limited numbers of events after the full selection. We extract the shapes of the distributions of these backgrounds from a control region in the data, similar to the signal region, but requiring no b-tagged jet in the event. In this selection the contribution of $t\bar{t}$ events is estimated to be about 15%. The remaining fraction consists of multijet, DY, and W boson events. The reconstruction algorithm is exactly the same as for the signal selection. To estimate the shape dependency in the control region on the selection we vary the selection threshold of the b-identification discriminant. This changes the top quark contribution and the flavor composition, however, we find the observed shape variation to be negligible. For the background subtraction, the distributions extracted from the control region are normalized individually in each bin of jet multiplicity to the yield of multijet, DY, and W boson events predicted by the simulation in the signal region. In the control region the expected and measured event yields agree within their statistical uncertainties. Taking into account the statistical uncertainty of the normalization factor and the shape differences between the signal and control regions in the simulation, we estimate an overall uncertainty of 20% in this background estimation.

Special care has to be taken with the contribution of nonsignal $t\bar{t}$ events. For the parton-level measurement these are dilepton, all-jets, and τ+jets events. For the particle-level measurement all $t\bar{t}$ events for which no pair of particle-level top quarks exists are considered as nonsignal $t\bar{t}$ events. The corresponding contributions are about 11.5% for the parton- and the particle-level measurements. The behavior of these backgrounds depend on the $t\bar{t}$ cross section and a subtraction according to the expected value can result in a bias of the measurement, especially if large differences between the simulation and the data are observed. However, the shapes of the distributions show an agreement within uncertainties between data and simulation and we subtract the predicted relative fractions from the remaining event yields.

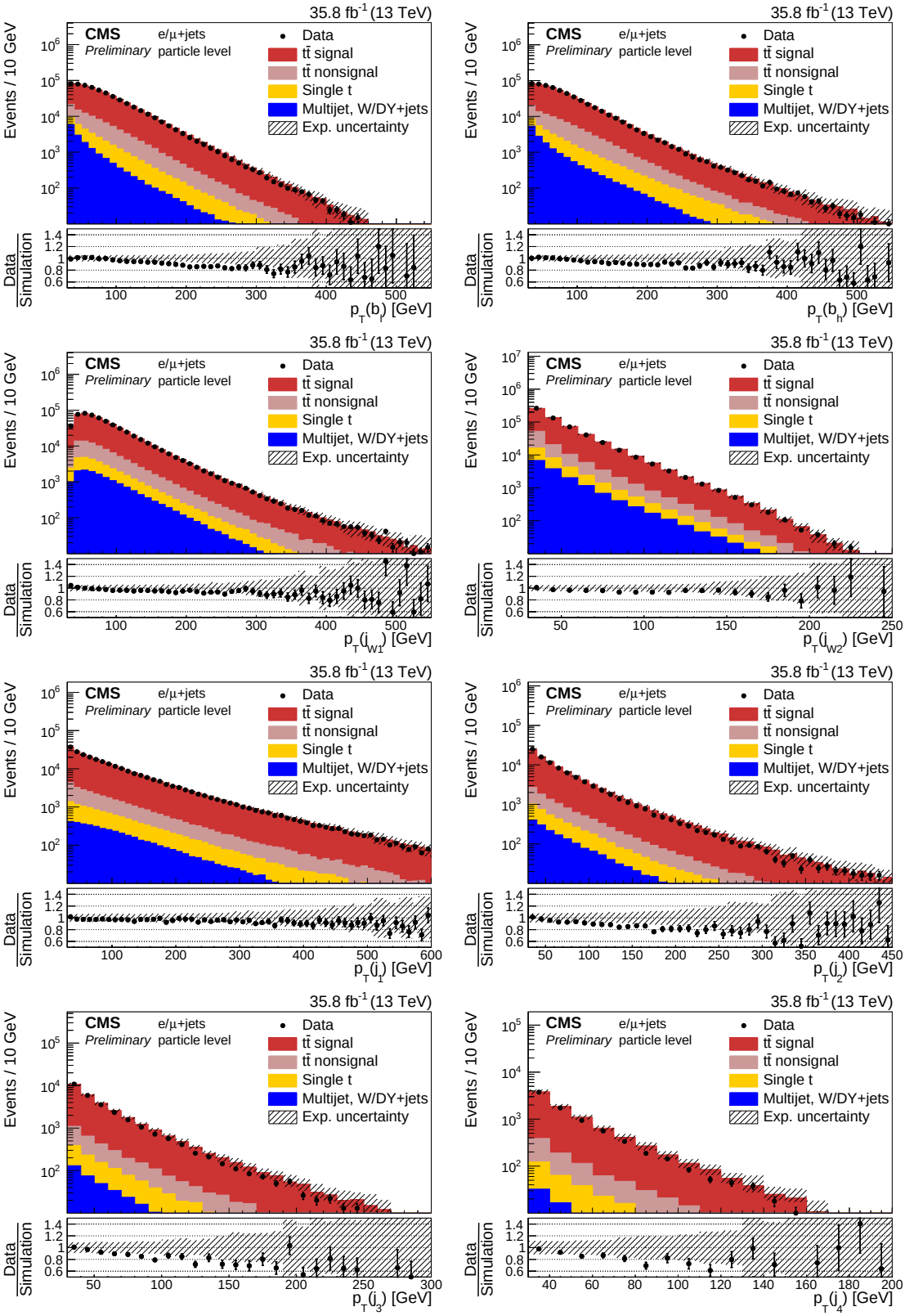

Figure 5: Comparisons of the reconstructed distributions of the p_T of jets as identified by the $t\bar{t}$ reconstruction algorithm. The simulation of POWHEG+PYTHIA8 is used to describe the $t\bar{t}$ production. The contribution of multijet, DY, and W boson events is extracted from the data (cf. Section 7). Experimental (cf. Section 9) and statistical uncertainties (hatched area) are shown for the total simulated yield, which is normalized according to the measured integrated luminosity of the data. The data points are shown with statistical uncertainties. The ratios of data to the expected yields are given at the bottom of each panel.

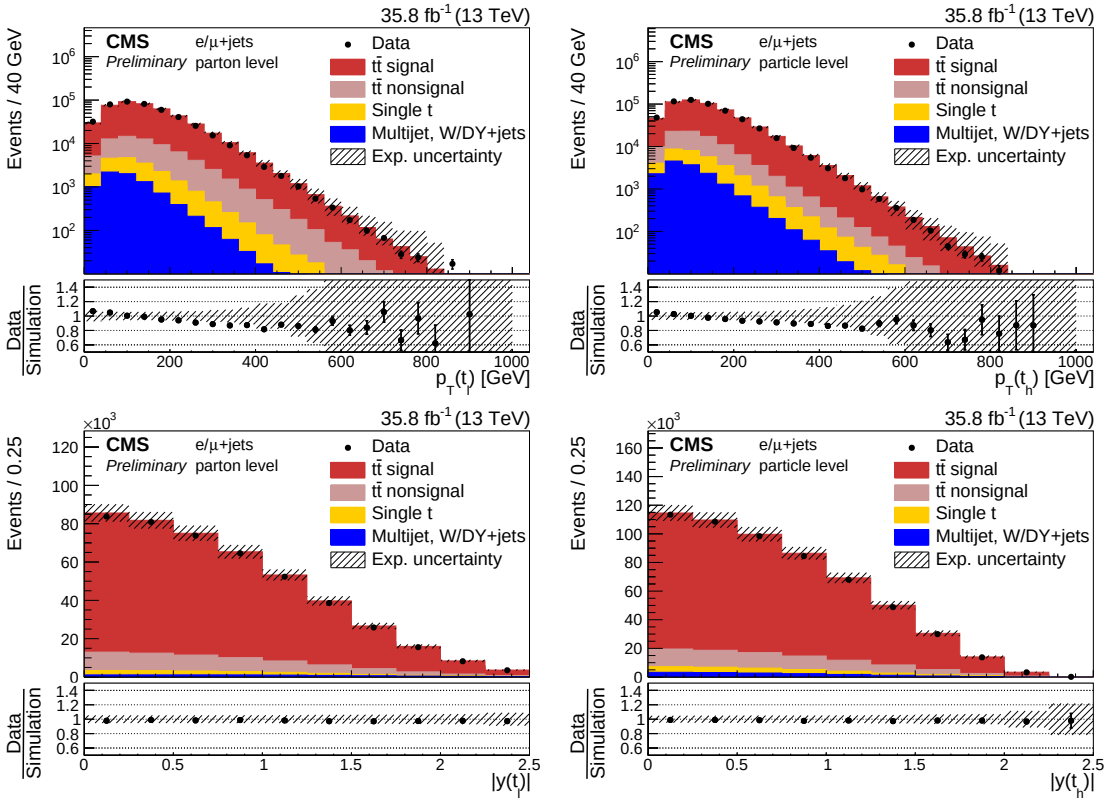

Figure 6: Comparisons of the reconstructed p_{T} (top) and $|y|$ (bottom) in data and simulations for the parton (left) and the particle (right) level. The simulation of POWHEG+PYTHIA8 is used to describe the $\mathrm{t\bar{t}}$ production. The contribution of multijet, DY, and W boson events is extracted from the data (cf. Section 7). Experimental (cf. Section 9) and statistical uncertainties (hatched area) are shown for the total simulated yield, which is normalized according to the measured integrated luminosity of the data. The data points are shown with statistical uncertainties. The ratios of data to the expected yields are given at the bottom of each panel.

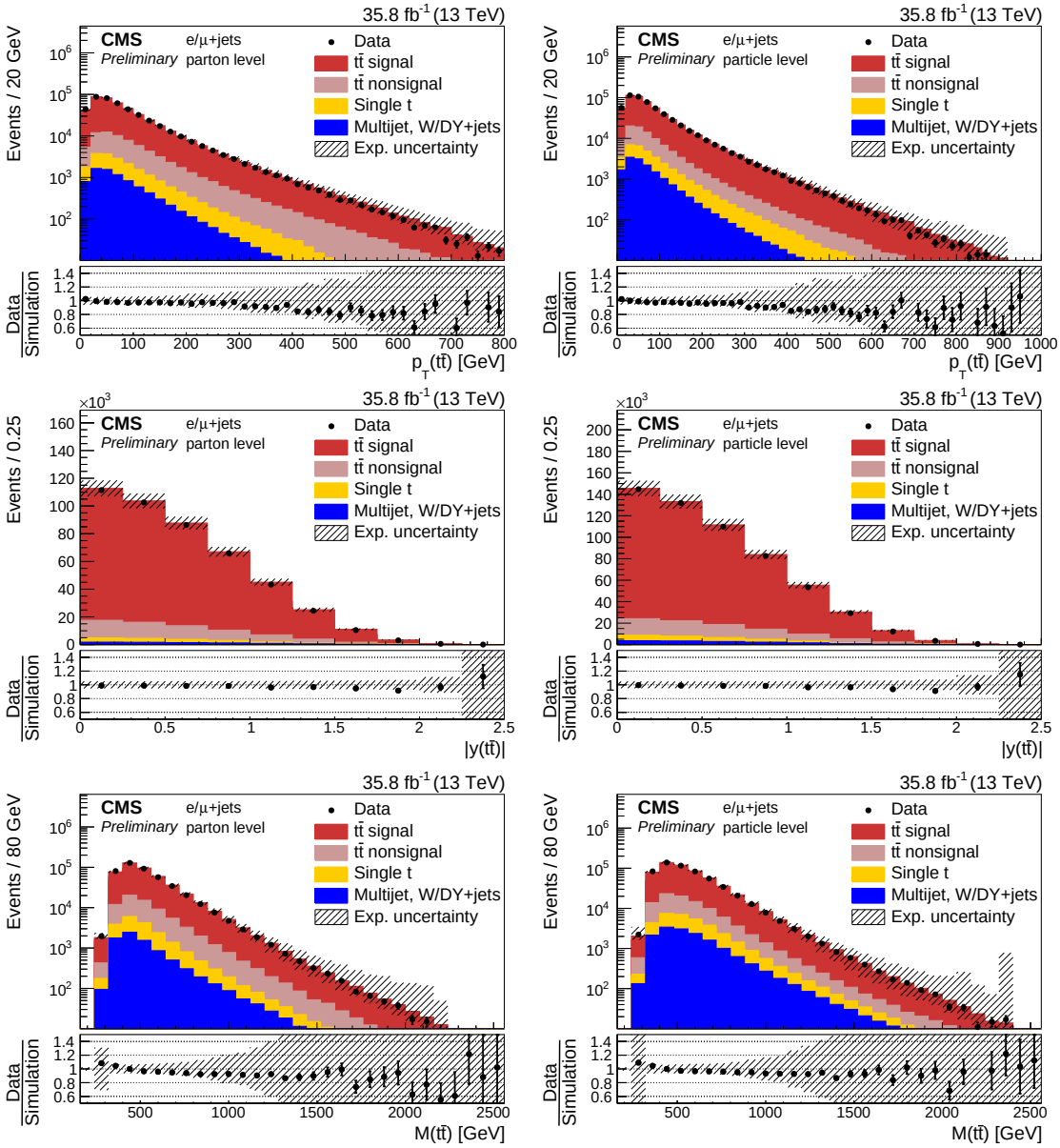

Figure 7: Comparisons of the reconstructed distributions of $p_{\mathrm{T}}(\mathrm{t\bar{t}})$ (top) and $M(\mathrm{t\bar{t}})$ (middle) for the parton- (left) and the particle- (right) level measurements in data and simulations. Bottom: distributions of $|y(\mathrm{t\bar{t}})|$ (left) and the number of additional jets (right). The simulation of POWHEG+PYTHIA8 is used to describe the $\mathrm{t\bar{t}}$ production. The contribution of multijet, DY, and W boson events is extracted from the data (cf. Section 7). Experimental (cf. Section 9) and statistical uncertainties (hatched area) are shown for the total simulated yield, which is normalized according to the measured integrated luminosity of the data. The data points are shown with statistical uncertainties. The ratios of data to the expected yields are given at the bottom of each panel.

8 Corrections applied for detector effects and extrapolation of the measurements

An unfolding procedure is used to correct the reconstructed distributions for detector specific effects, e.g, efficiencies and resolutions, and to extrapolate either to the parton or particle level. For the unfolding, the iterative D'Agostini method [43] is used. The migration matrices and the acceptances are needed as input. The migration matrix relates the quantities at parton (particle) level and at detector level. It accounts for the effects from the parton shower and hadronization as well as the detector response, where the former has a large impact on the parton-level measurement. For the central results the migration matrices and the acceptances are taken from the POWHEG+PYTHIA8 simulation and other simulations are used to estimate the uncertainties. The binning in the unfolding is optimized based on the resolution in the simulation. We utilize for the minimal bin widths that, according to the resolution, at least 50% of the events are reconstructed in the correct bin. In Fig. 8 as an example the migration matrices of the parton- and particle-level measurements of $p_{\mathrm{T}}(\mathrm{t_h})$ are shown together with the fraction of parton- (particle-) level top quarks in the same bin at detector level (purity), fraction of detector-level top quarks in the same bin at parton (particle) level (stability), and ratio of the number of detector- to parton- (particle-) level top quarks (bin efficiency). These illustrate the improved agreement between the detected and the unfolded quantity as well as the reduced extrapolation in the particle-level measurement.

The iterative D'Agostini method takes the number of iterations as an input parameter to control the level of regularization. To optimize the number of iterations, we chose the criterion that the compatibility between a model and the unfolded data at parton (particle) level is the same as the compatibility between the folded model and the data at detector level. The compatibilities are determined by χ^2 tests at both levels based on all available simulations and several modified spectra obtained by reweighting the $p_{\mathrm{T}}(\mathrm{t})$, $|y(\mathrm{t})|$, $p_{\mathrm{T}}(\mathrm{t\bar{t}})$, or $p_{\mathrm{T}}(\mathrm{j_1})$ distributions in the POWHEG+PYTHIA8 simulation. The reweighted spectra are chosen in such a way that they cover the observed differences between the data and the unmodified simulation at detector level.

We find the above criterion fulfilled for the number of iterations such that a second χ^2 test between the detector-level spectrum with its statistical uncertainty and the refolded spectrum exceeds a probability of 99.9%. The refolded spectrum is obtained by inverting the unfolding step. This consists of a multiplication with the response matrix and does not need any regularization. We take the initial distributions for the D'Agostini unfolding from the POWHEG+PYTHIA8 simulation. The algorithm needs between 4 and 56 iterations depending on the distribution. The numbers of iterations are higher for measurements with lower purities and stabilities of the migration matrices. This is the case for the measurements of $p_{\mathrm{T}}(\mathrm{t}_\ell)$ and $|y(\mathrm{t}_\ell)|$ whose resolutions are significant lower than those of $p_{\mathrm{T}}(\mathrm{t_h})$ and $|y(\mathrm{t_h})|$ due to the missing neutrino information.

For the two-dimensional measurements with n bins in one and m bins in the other quantity the D'Agostini unfolding can be generalized using a vector of $n \cdot m$ entries of the form: $b_{1,1}, b_{2,1} \ldots b_{n,1}, \ldots b_{1,m}, b_{2,m} \ldots b_{n,m}$ with a corresponding $(n \cdot m) \times (n \cdot m)$ migration matrix. The number of iterations is optimized in the same way.

In the measurements of kinematic properties of jets we do not unfold the measured spectra of each jet separately, but also correct for the effect of misidentified jets. The response matrix showing the migration among the identified jets is shown in Fig. 9 for the measurements of the jet p_{T} spectra.

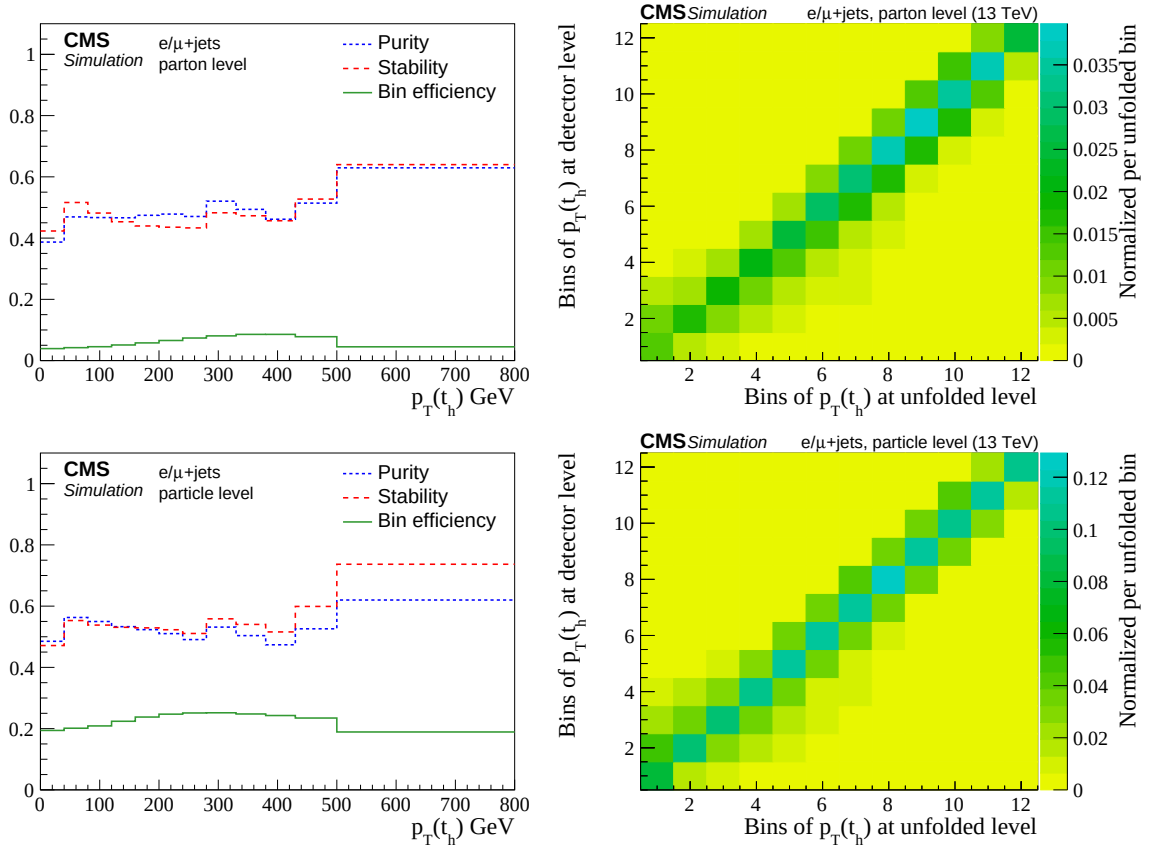

Figure 8: Migration studies of the parton (top) and particle (bottom) level measurements of $p_T(t_h)$, extracted from the POWHEG+PYTHIA8 simulation. Left: purity, stability, and efficiency per bin. Right: bin migrations between detector and parton (particle) level. The p_T range of the bins can be taken from the left panels. Each column is normalized to the number of events per column at parton (particle) level in the finally measured phase space.

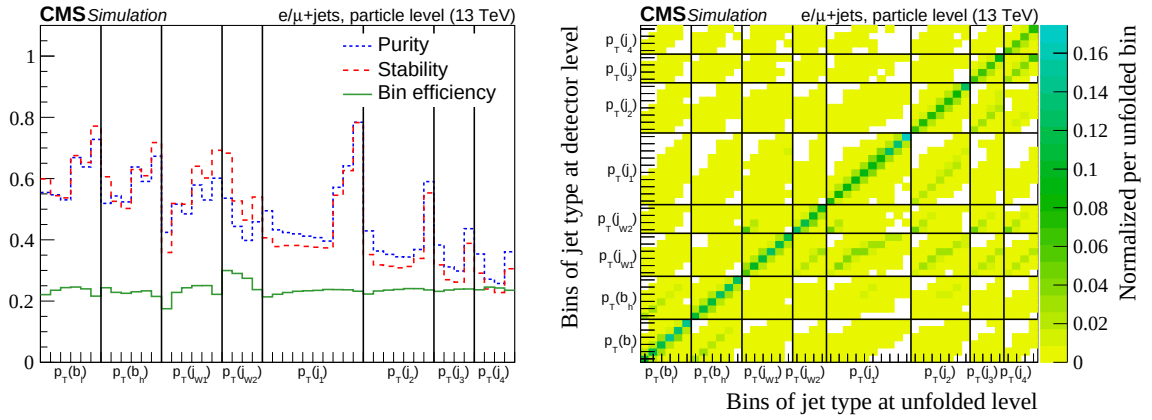

Figure 9: Migration matrices of the particle level measurement of the jet p_T spectra, extracted from the POWHEG+PYTHIA8 simulation. Left: purity, stability, and efficiency per bin. Right: bin migrations between detector and particle level. On the axes the p_T bins for each jet are shown. Each column is normalized to the number of events per column at particle level.

9 Systematic uncertainties

We study several sources of experimental and theoretical uncertainty. Uncertainties in the jet and $\vec{p}_{\mathrm{T}}^{\,\mathrm{miss}}$ calibrations, in the pileup modeling, in the b identification and lepton selection efficiencies, and in the integrated luminosity measurement fall into the first category.

The total uncertainties in the jet energy calibration is the combination of 19 different sources of uncertainty and the jet flavor specific uncertainties [40], where the uncertainty for b jets is evaluated separately. According to each uncertainty source, the energies of jets in the simulation are shifted up and down. At the same time $\vec{p}_{\mathrm{T}}^{\,\mathrm{miss}}$ is recalculated according to the rescaled jet energies. The recomputed backgrounds, response matrices, and acceptances are used to unfold the data. The observed differences between these and the original results are taken as an uncertainty in the unfolded event yields. The same technique is used to calculate the impact of the uncertainties in the jet energy resolution, the uncertainty in $\vec{p}_{\mathrm{T}}^{\,\mathrm{miss}}$ not related to the jet energy calibration, in the b identification, and in the pileup modeling.

The b identification efficiency in the simulation is corrected using scale factors determined from the data [41]. These have an uncertainty of about 1–3% depending on the p_{T} of the b jet.

The effect on the measurement due to the uncertainty in the modeling of pileup in the simulation is estimated by varying the average number of pileup events per bunch crossing by 4.6% and reweighting the simulated events accordingly.

The trigger, reconstruction, and identification efficiencies of leptons are evaluated with tag-and-probe techniques using Z boson dilepton decays [37, 39]. The uncertainties in the scale factors, which are used to correct the simulation to match the data, take into account the different lepton selection efficiencies in events with high jet multiplicities as in $\mathrm{t\bar{t}}$ events. The overall uncertainty in the lepton reconstruction and selection efficiencies depends on p_{T} and η and is about 2%.

The relative uncertainty in the integrated luminosity measurement is 2.5% [1].

Uncertainties in the choice of factorization and renormalization scales, the combination of the matrix element calculation with the parton shower, the modeling of the parton shower and hadronization, the top quark mass, and the PDFs fall into the second category of uncertainties. The effects of these theoretical uncertainties are estimated either by using the various event weights introduced in Section 2, or by using a $\mathrm{t\bar{t}}$ signal simulation with varied settings. Again, the uncertainties are assessed using the recomputed backgrounds, response matrices, and acceptances to unfold the data.

The factorization and renormalization scales are varied up and down by a factor of two individually and simultaneously in the same directions. Afterwards the envelope of the observed variations is quoted as uncertainty.

The uncertainty in the combination of the matrix element calculation with the parton shower is estimated from an $\approx$40% variation of the h_{damp} parameter in POWHEG, normally set to $h_{\mathrm{damp}} = 1.58 m_{\mathrm{t}}$. This variation has been found to be compatible with the modelling of jet multiplicities in the LHC Run I data [10].

To estimate the uncertainty in the parton shower several effects have been studied and are assessed individually. The scale of the initial- (final-) state radiation is varied up and down by a factor of two ($\sqrt{2}$). These variations are motivated by the uncertainties of parton-shower tuning [23]. The effect of multiple-parton interactions and the parameterization of color reconnection have been studied in [44] and are varied accordingly. In addition, we use a simulation

with activated color reconnection of resonant decays. The uncertainty in the b fragmentation function is taken from measurements at LEP and SLD and the parameterization in PYTHIA8 is changed accordingly. Finally, the semi-leptonic branching fraction [45] of b hadrons is varied within their measured uncertainties.

The effect due to uncertainties in the top quark mass is estimated using simulations with altered top quark masses. We quote as uncertainty the cross section differences observed for a top quark mass variation of 1 GeV around the central value of 172.5 GeV used in the central simulation.

For the PDF uncertainty only the variation in the acceptance is taken into account, while variations due to migrations between bins are neglected. It is calculated according to the uncertainties in the NNPDF30_nlo_as_0118 [25] parametrization. In addition, the uncertainties obtained using the PDF sets derived with varied values of the strong coupling constant, $\alpha_s = 0.117$ and 0.119, are considered.

As an example, the sources of uncertainty in the measurements of $p_T(t_h)$ are shown in Fig. 10. Among the experimental uncertainties the dominant sources are the jet energy scale; lepton triggering, reconstruction, and identification; and the b identification. In the parton-level measurement the choice of scale for final-state radiation has typically a dominant contribution.

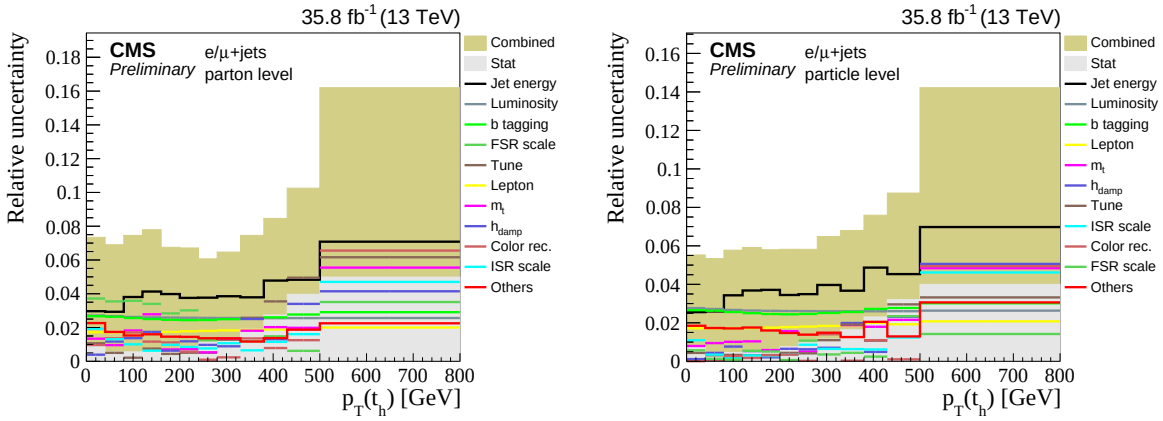

Figure 10: Relative uncertainties due to the individual sources in the measurement of $p_T(t_h)$ at parton level (left) and particle level (right). Sources of a maximum uncertainty below 0.5% are summarized in the category "Others". The combination of the individual sources of jet energy uncertainty is labeled "Jet energy". The combined uncertainty considers all systematic uncertainties.

As an additional consistency test, we unfold the data using the reweighted simulations that envelope all differences in the measured distributions at detector level described in Section 8. The differences between these unfolded distributions and the one obtained with the unmodified simulation are small compared to the uncertainties evaluated by the variations described above.

10 Differential cross sections as a function of observables of the top quark and the top quark-antiquark system

The cross section σ in each bin is calculated as the ratio of the unfolded signal yield and the integrated luminosity. These are further divided by the bin width (the product of the two bin widths) to obtain the single- (double-) differential results.

The measured differential cross sections are compared to the predictions of POWHEG combined with the parton-shower simulations of PYTHIA8 and HERWIG++ and the $t\bar{t}$ multiparton simulation of MG5_aMC@NLO+PYTHIA8 FxFx. In addition, several parton-level results are compared to calculations of $t\bar{t}$ production with NNLO QCD+NLO electroweak (EW) [46] accuracy. A top quark mass of 173.3 GeV is used. For the calculations as function of $M(t\bar{t})$ and rapidities the renormalization and factorization scales are set to $\frac{1}{4}\left(\sqrt{m_t^2 + p_T^2(t)} + \sqrt{m_t^2 + p_T^2(\bar{t})}\right)$, for the transverse momenta the scales are set to $\frac{1}{2}\sqrt{m_t^2 + p_T^2}$, where p_T is the transverse momentum of t, $\bar{t}$, t_{high}, or t_{low} depending on the variable under consideration. The PDF parametrizations LUXqed_plus_PDF4LHC15_nnlo_100 [47] are used for these calculations. The uncertainties consider variations of the renormalization and factorization scales. The particle-level results are compared to a prediction obtained with the Monte Carlo generator SHERPA [48] (v2.2.3) in combination with OPENLOOPS [49]. The processes of $t\bar{t}$ production with up to one additional jet are calculated at NLO QCD accuracy, $t\bar{t}$ production with up to four additional jets are calculated at LO. These processes are merged and matched with the CS parton shower [50] based on the SHERPA default tune. The NNPDF30_nlo_as_0118 [25] PDF parametrizations are used. Uncertainties in the predictions of SHERPA are evaluated by halving and doubling the scales of renormalization, factorization, resummation, and the initial- and final-state parton shower. In addition, the PDF uncertainties are taken into account. For the predictions of POWHEG+PYTHIA8 we evaluate all theoretical uncertainties as described in Section 9. The comparisons are shown in Fig. 11 (12) as a function of the top quark p_T and $|y|$ at parton (particle) level. At parton level the kinematic properties of t_h and t_ℓ are identical and we measure the differential cross section as a function of p_T of the top quark with the higher and lower p_T. The measured p_T spectra of t_h and t_ℓ are consistently softer than predicted by the simulations including the PYTHIA8 parton shower at particle and parton level. The POWHEG+HERWIG++ simulation follows the data at parton level. However, at particle level it shows an opposite behavior with respect to the PYTHIA8 simulation and predicts softer spectra. In Figs. 13 and 14 the cross sections as a function of kinematic variables of the $t\bar{t}$ system are compared to the same theoretical predictions. These follow the measured distributions consistently. Only for $M(t\bar{t})$ at particle level the PYTHIA8 and HERWIG++ simulations behave differently.

The measurement of double-differential cross sections allows for the study of correlations between kinematic properties of the top quarks and provides insights into extreme regions of the phase space. The most fundamental double-differential distribution is the measurement of the top quark properties $|y(t_h)|$ *vs.* $p_T(t_h)$ shown in Fig. 15 (16) at parton (particle) level. The observation of a softer $p_T(t)$ spectrum is persistent in all rapidity regions. In Figs. 17 and 18 the measurements of $M(t\bar{t})$ *vs.* $|y(t\bar{t})|$ are shown. This distribution is sensitive to the extraction of PDFs. With increasing $M(t\bar{t})$ the simulations overestimate the cross sections at high $|y(t\bar{t})|$. This observation is consistent at particle and parton level. Finally, we measure $p_T(t_h)$ *vs.* $M(t\bar{t})$ shown in Figs. 19 and 20. These demonstrates the increasingly harder $M(t\bar{t})$ spectrum at higher $p_T(t_h)$.

The precision of the measurement is limited by systematic uncertainties, dominated by jet energy scale uncertainties on the experimental side and parton shower modeling and scale uncertainties on the theoretical side. As expected, the theoretical uncertainties are reduced in the particle-level measurements since these are less dependent on theory-based extrapolations.

We evaluate the level of agreement between the measured differential cross sections and the various theoretical predictions using χ^2 tests. In these tests we take into account the full covariance matrices of the measured differential cross sections. For the statistical uncertainty the covariances are taken directly from the unfolding procedure. For each of the studied system-

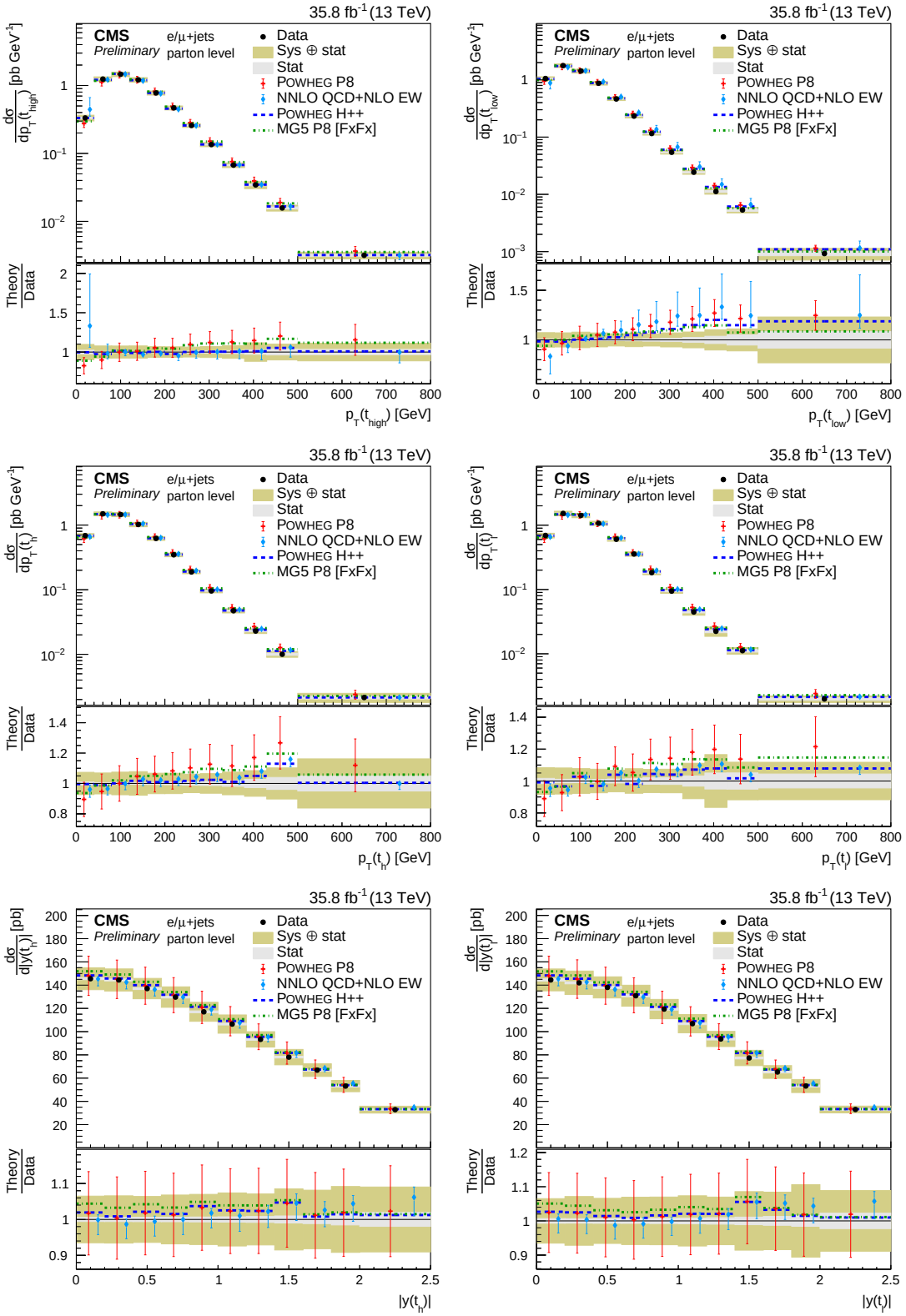

Figure 11: Differential cross sections at parton level as a function of the top quark with the higher and lower p_T (top), $p_T(t_h)$and $p_T(t_\ell)$ (middle), and $|y(t_h)|$ and $|y(t_\ell)|$ (bottom). The data are shown as points with light (dark) error bands indicating the statistical (statistical and systematic) uncertainties. The cross sections are compared to the predictions of POWHEG combined with PYTHIA8 (P8) or HERWIG++ (H++), the multiparton simulation MG5_aMC@NLO (MG5)+PYTHIA8 FxFx, and the NNLO QCD+NLO EW calculations. The ratios of the various predictions to the measured cross sections are shown at the bottom of each panel.

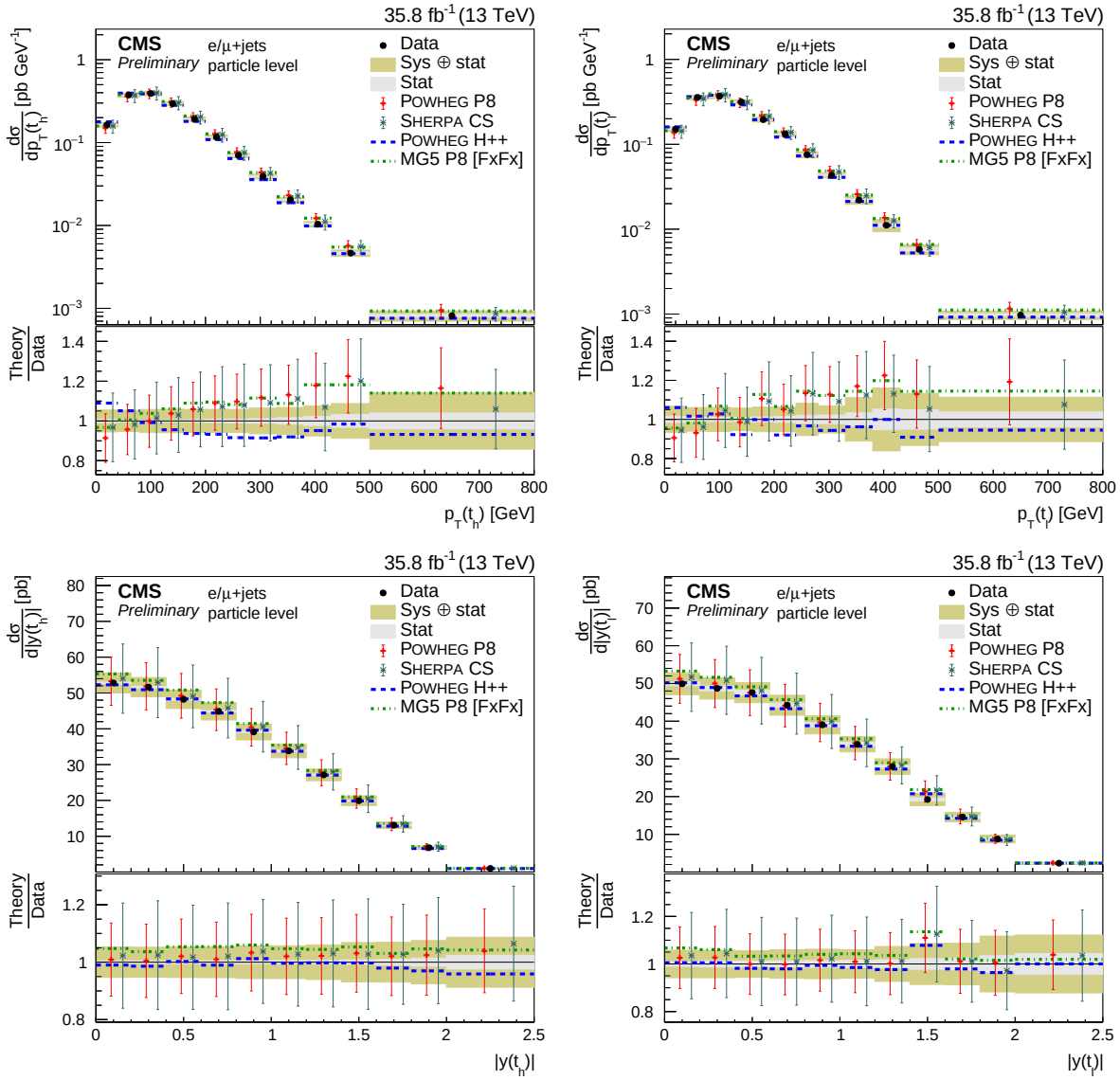

Figure 12: Differential cross sections at particle level as a function of $p_{\mathrm{T}}(\mathrm{t})$ (top) and $|y(\mathrm{t})|$ (bottom) measured separately for the hadronically (left) and leptonically (right) decaying particle-level top quarks. The data are shown as points with light (dark) error bands indicating the statistical (statistical and systematic) uncertainties. The cross sections are compared to the predictions of POWHEG combined with PYTHIA8 (P8) or HERWIG++ (H++) and the multiparton simulations MG5_aMC@NLO (MG5)+PYTHIA8 FxFx and SHERPA. The ratios of the various predictions to the measured cross sections are shown at the bottom of each panel.

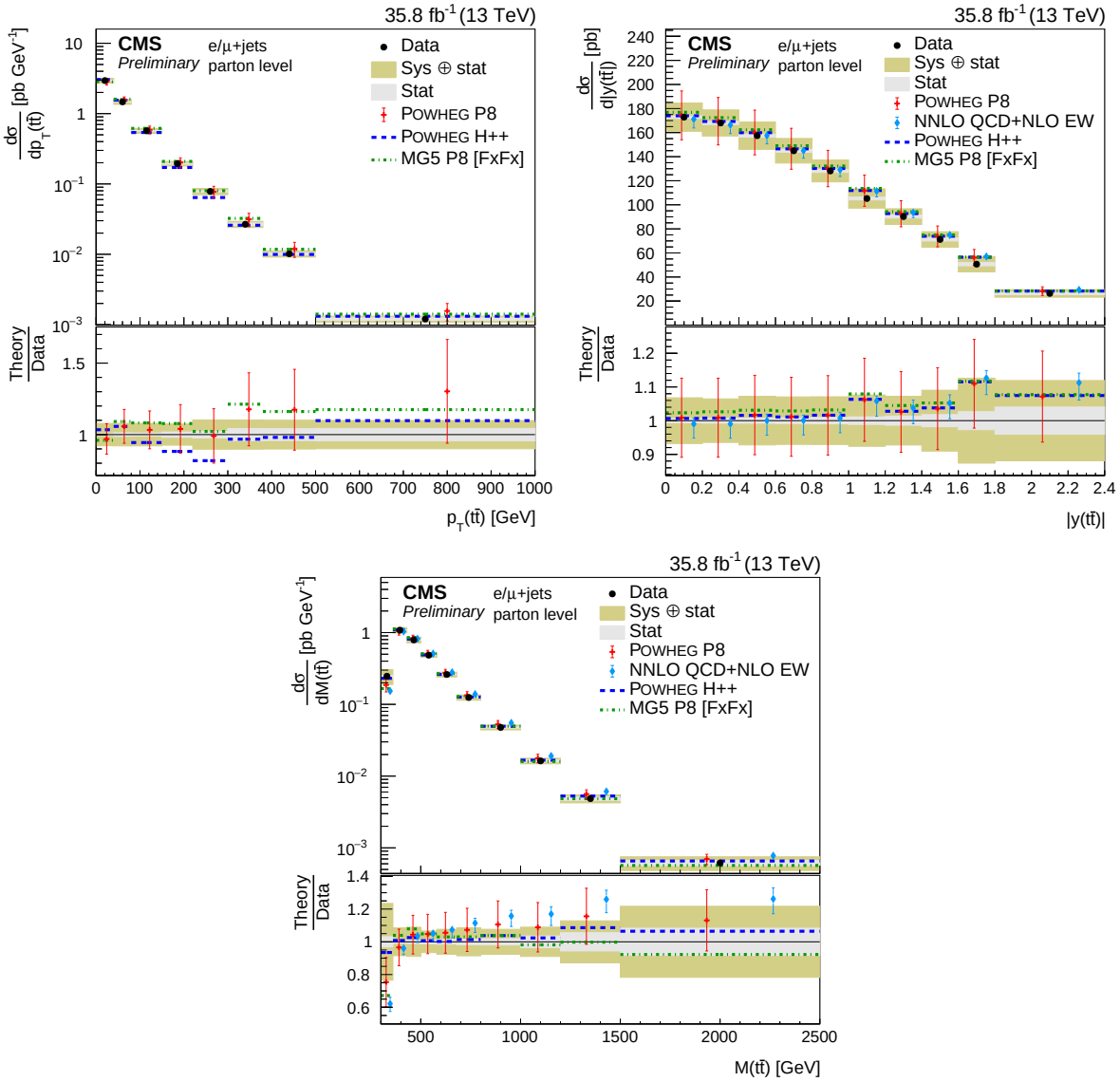

Figure 13: Differential cross sections at parton level as a function of $p_{\mathrm{T}}(\mathrm{t\bar{t}})$, $|y(\mathrm{t\bar{t}})|$, and $M(\mathrm{t\bar{t}})$. The data are shown as points with light (dark) error bands indicating the statistical (statistical and systematic) uncertainties. The cross sections are compared to the predictions of POWHEG combined with PYTHIA8 (P8) or HERWIG++ (H++), the multiparton simulations MG5_aMC@NLO (MG5)+PYTHIA8 FxFx, and the NNLO QCD+NLO EW calculations. The ratios of the various predictions to the measured cross sections are shown at the bottom of each panel.

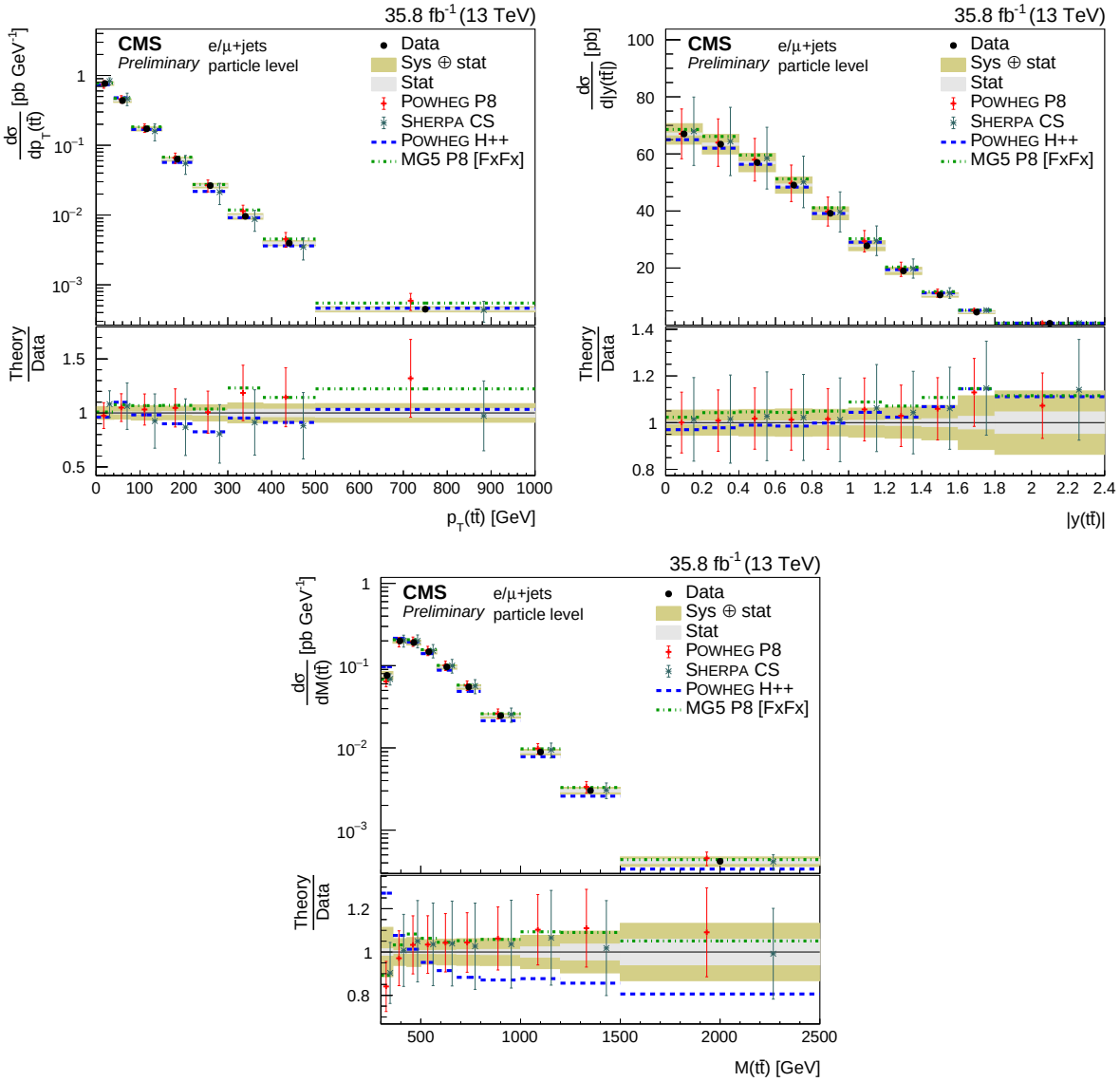

Figure 14: Differential cross sections at particle level as a function of $p_{\mathrm{T}}(\mathrm{t\bar{t}})$, $|y(\mathrm{t\bar{t}})|$, and $M(\mathrm{t\bar{t}})$. The data are shown as points with light (dark) error bands indicating the statistical (statistical and systematic) uncertainties. The cross sections are compared to the predictions of POWHEG combined with PYTHIA8 (P8) or HERWIG++ (H++) and the multiparton simulations MG5_aMC@NLO (MG5)+PYTHIA8 FxFx and SHERPA. The ratios of the various predictions to the measured cross sections are shown at the bottom of each panel.

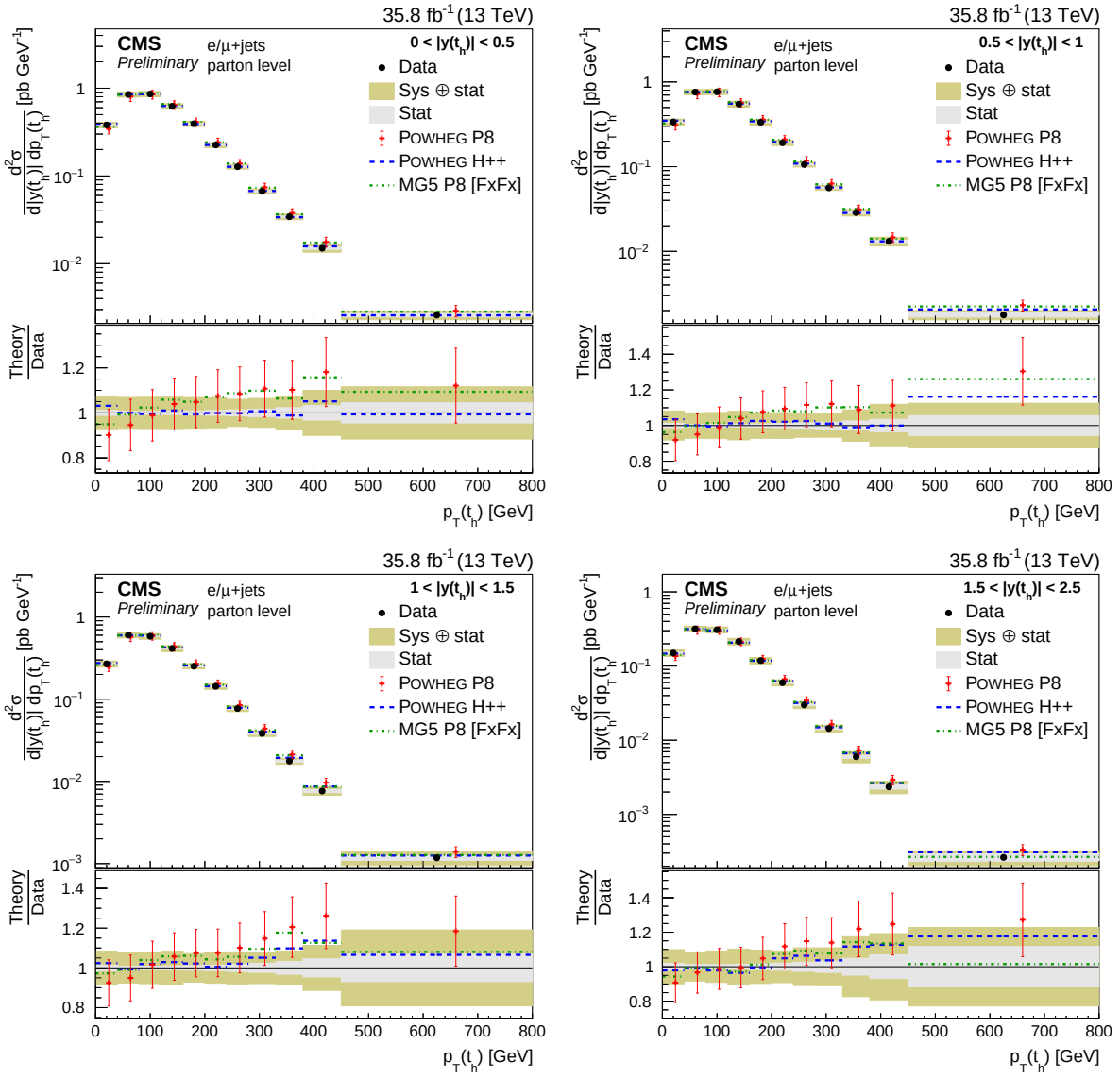

Figure 15: Double-differential cross section at parton level as a function of $|y(\mathrm{t_h})|$ *vs.* $p_\mathrm{T}(\mathrm{t_h})$. The data are shown as points with light (dark) error bands indicating the statistical (statistical and systematic) uncertainties. The cross sections are compared to the predictions of POWHEG combined with PYTHIA8 (P8) or HERWIG++ (H++) and the multiparton simulation MG5_aMC@NLO (MG5)+PYTHIA8 FxFx. The ratios of the predictions to the measured cross sections are shown at the bottom of each panel.

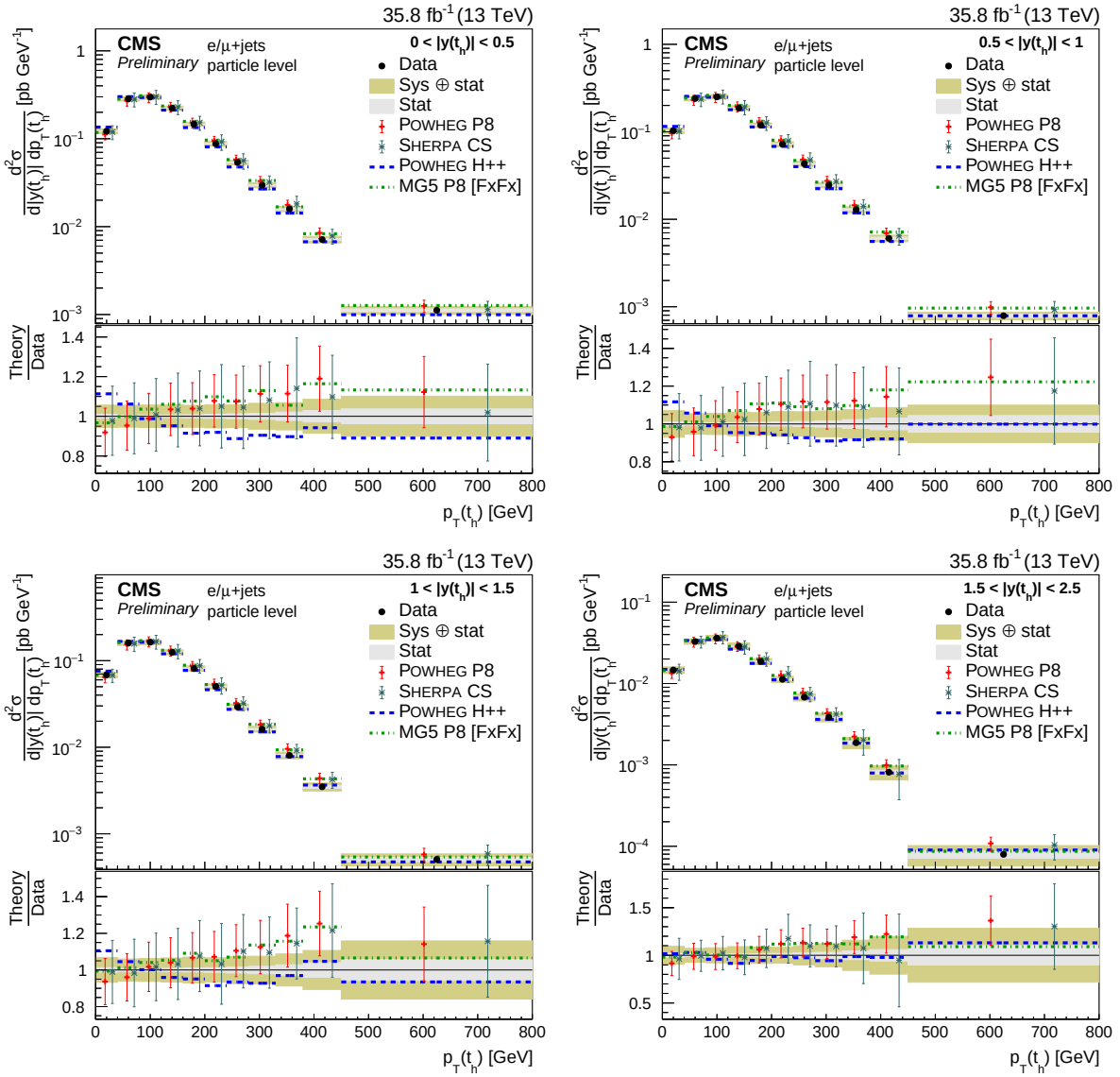

Figure 16: Double-differential cross section at particle level as a function of $|y(\mathrm{t_h})|$ *vs.* $p_\mathrm{T}(\mathrm{t_h})$. The data are shown as points with light (dark) error bands indicating the statistical (statistical and systematic) uncertainties. The cross sections are compared to the predictions of POWHEG combined with PYTHIA8 (P8) or HERWIG++ (H++) and the multiparton simulations MG5_aMC@NLO (MG5)+PYTHIA8 FxFx and SHERPA. The ratios of the predictions to the measured cross sections are shown at the bottom of each panel.

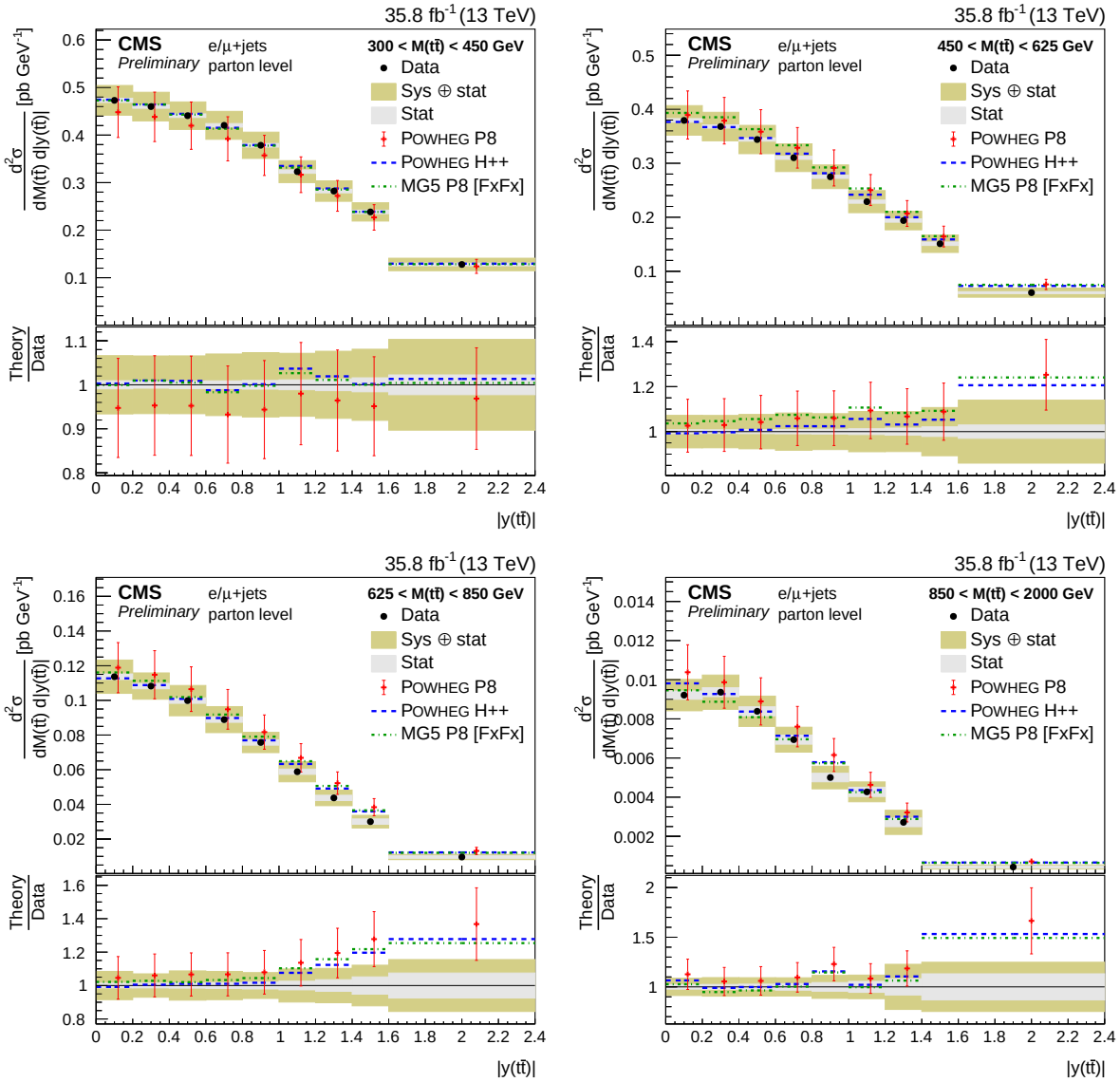

Figure 17: Double-differential cross section at parton level as a function of $M(\mathrm{t\bar{t}})$ *vs.* $|y(\mathrm{t\bar{t}})|$. The data are shown as points with light (dark) error bands indicating the statistical (statistical and systematic) uncertainties. The cross sections are compared to the predictions of POWHEG combined with PYTHIA8 (P8) or HERWIG++ (H++) and the multiparton simulation MG5_aMC@NLO (MG5)+PYTHIA8 FxFx. The ratios of the predictions to the measured cross sections are shown at the bottom of each panel.

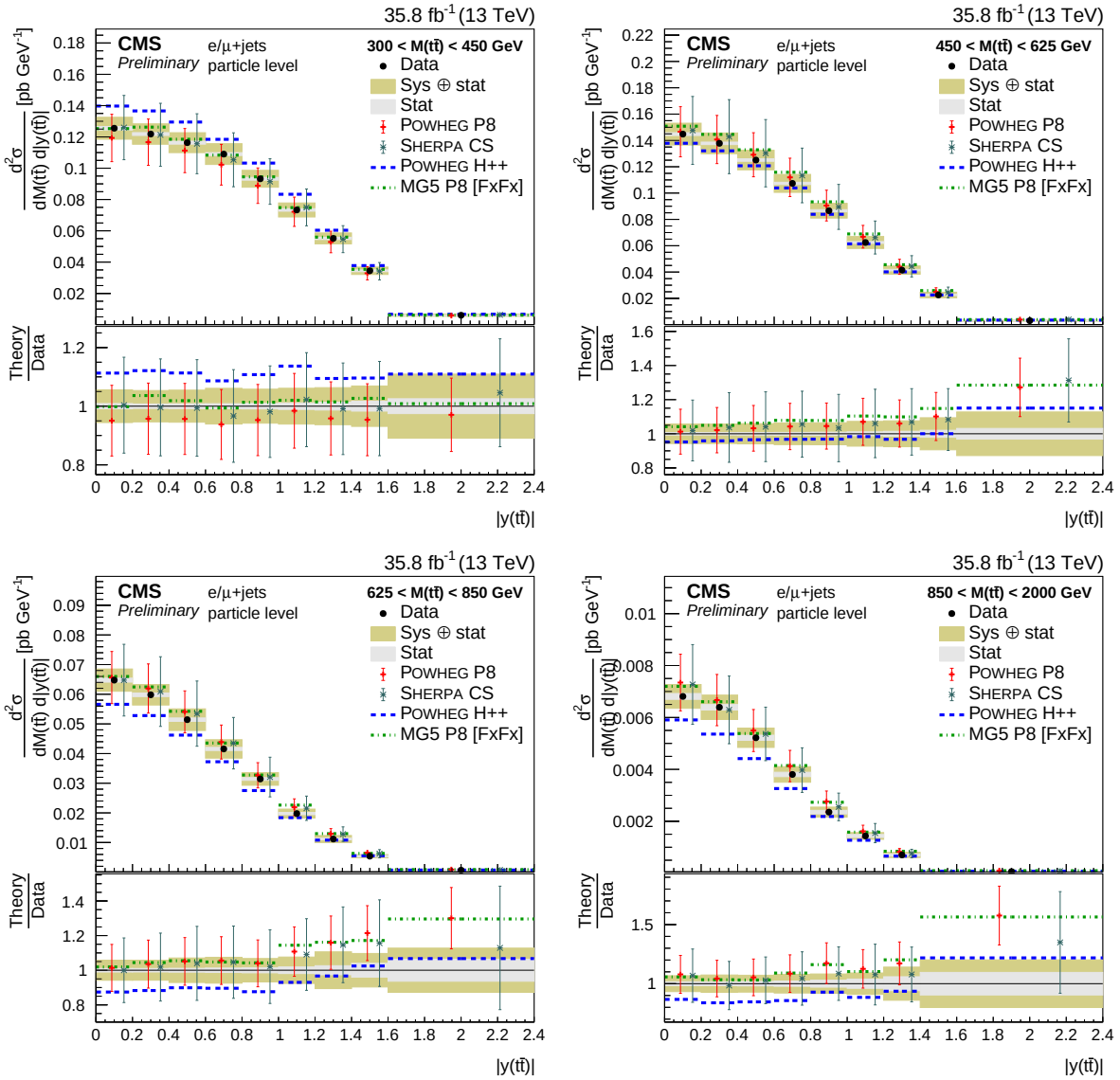

Figure 18: Double-differential cross section at particle level as a function of $M(\mathrm{t\bar{t}})$ *vs.* $|y(\mathrm{t\bar{t}})|$. The data are shown as points with light (dark) error bands indicating the statistical (statistical and systematic) uncertainties. The cross sections are compared to the predictions of POWHEG combined with PYTHIA8 (P8) or HERWIG++ (H++) and the multiparton simulations MG5_aMC@NLO (MG5)+PYTHIA8 FxFx and SHERPA. The ratios of the predictions to the measured cross sections are shown at the bottom of each panel.

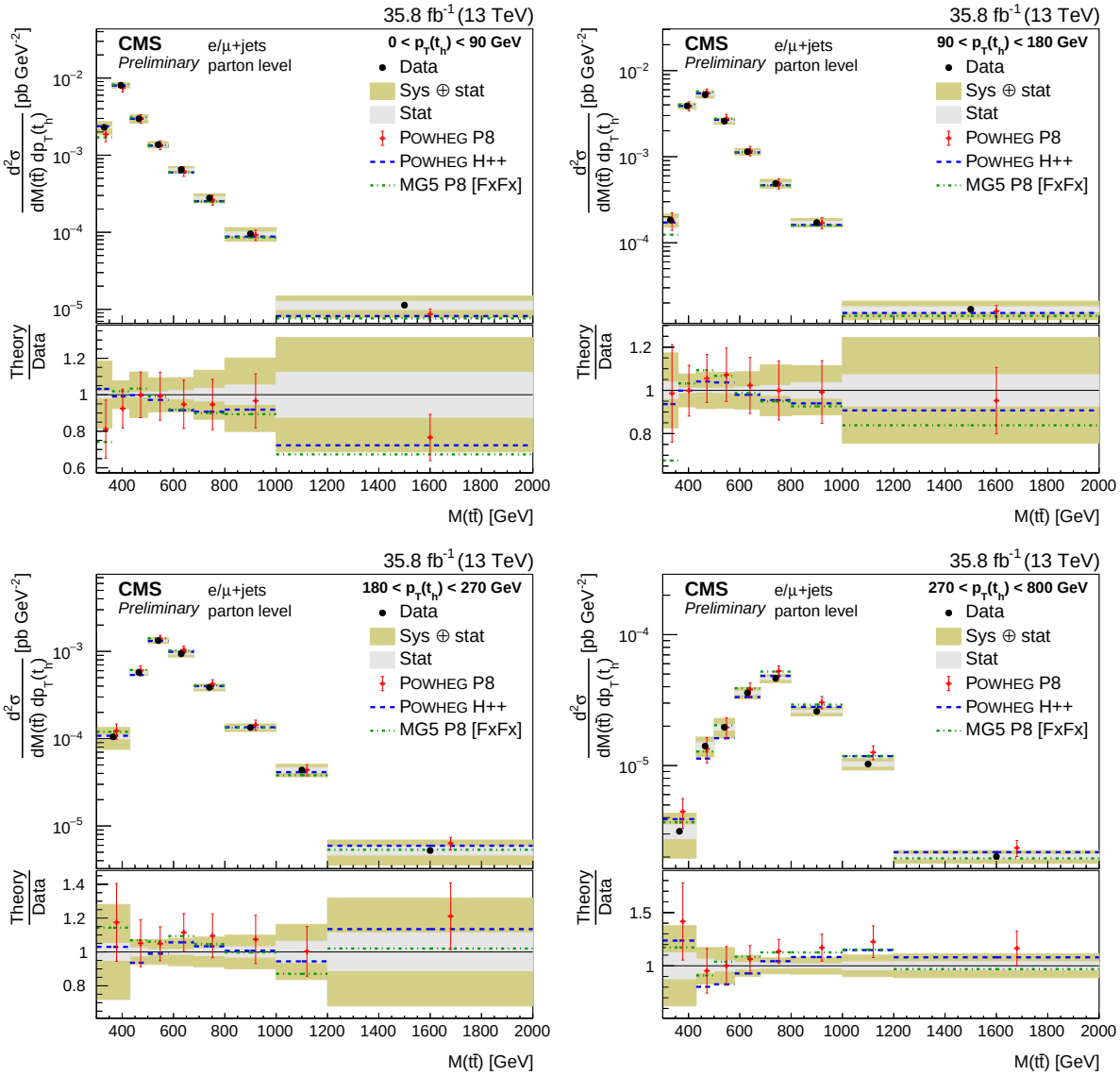

Figure 19: Double-differential cross section at parton level as a function of $p_T(t_h)$ *vs.* $M(t\bar{t})$. The data are shown as points with light (dark) error bands indicating the statistical (statistical and systematic) uncertainties. The cross sections are compared to the predictions of POWHEG combined with PYTHIA8 (P8) or HERWIG++ (H++) and the multiparton simulation MG5_aMC@NLO (MG5)+PYTHIA8 FxFx. The ratios of the predictions to the measured cross sections are shown at the bottom of each panel.

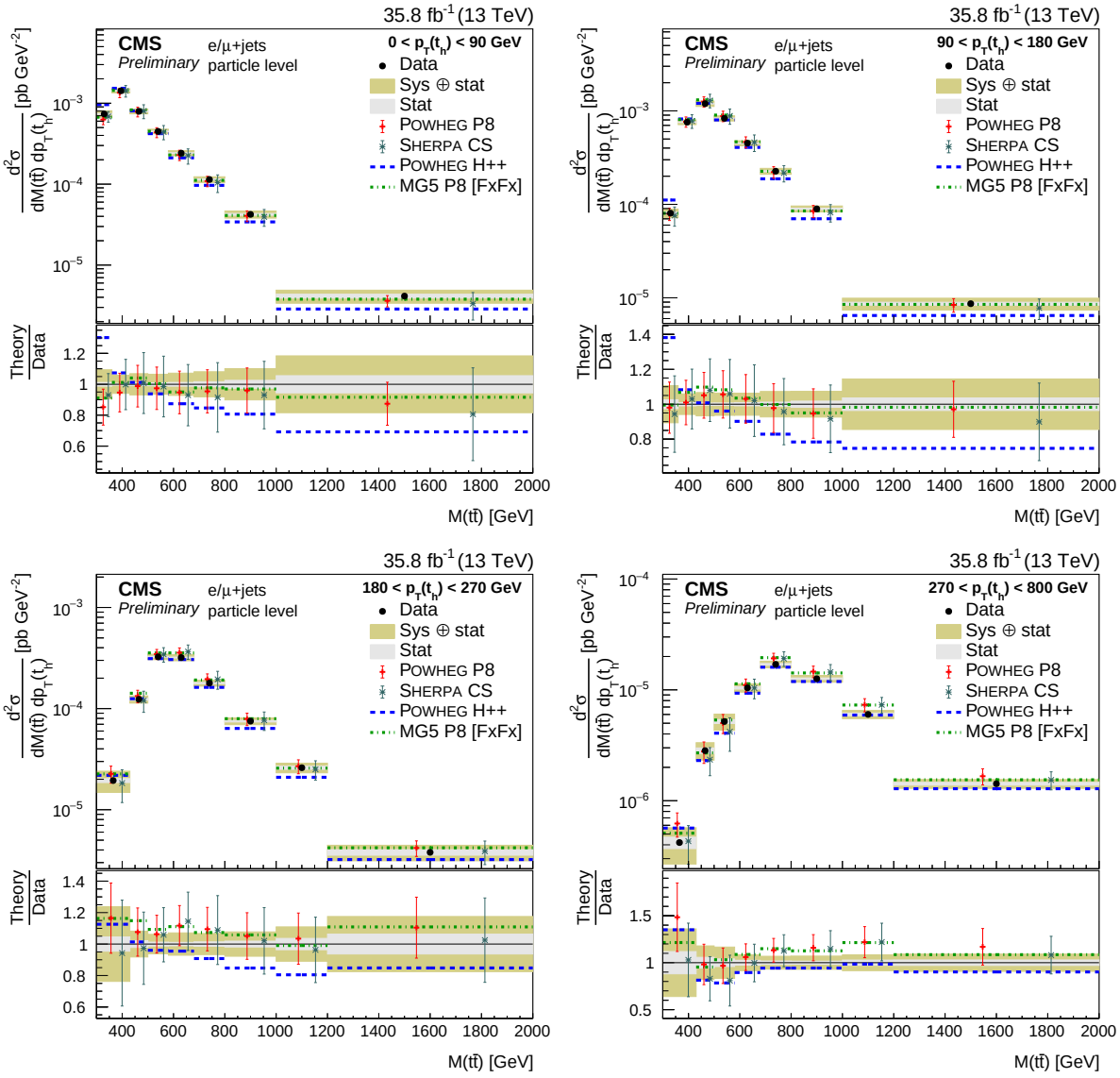

Figure 20: Double-differential cross section at particle level as a function of $|y(\mathrm{t\bar{t}})|$ *vs.* $M(\mathrm{t\bar{t}})$. The data are shown as points with light (dark) error bands indicating the statistical (statistical and systematic) uncertainties. The cross sections are compared to the predictions of POWHEG combined with PYTHIA8 (P8) or HERWIG++ (H++) and the multiparton simulations MG5_aMC@NLO (MG5)+PYTHIA8 FxFx and SHERPA. The ratios of the predictions to the measured cross sections are shown at the bottom of each panel.

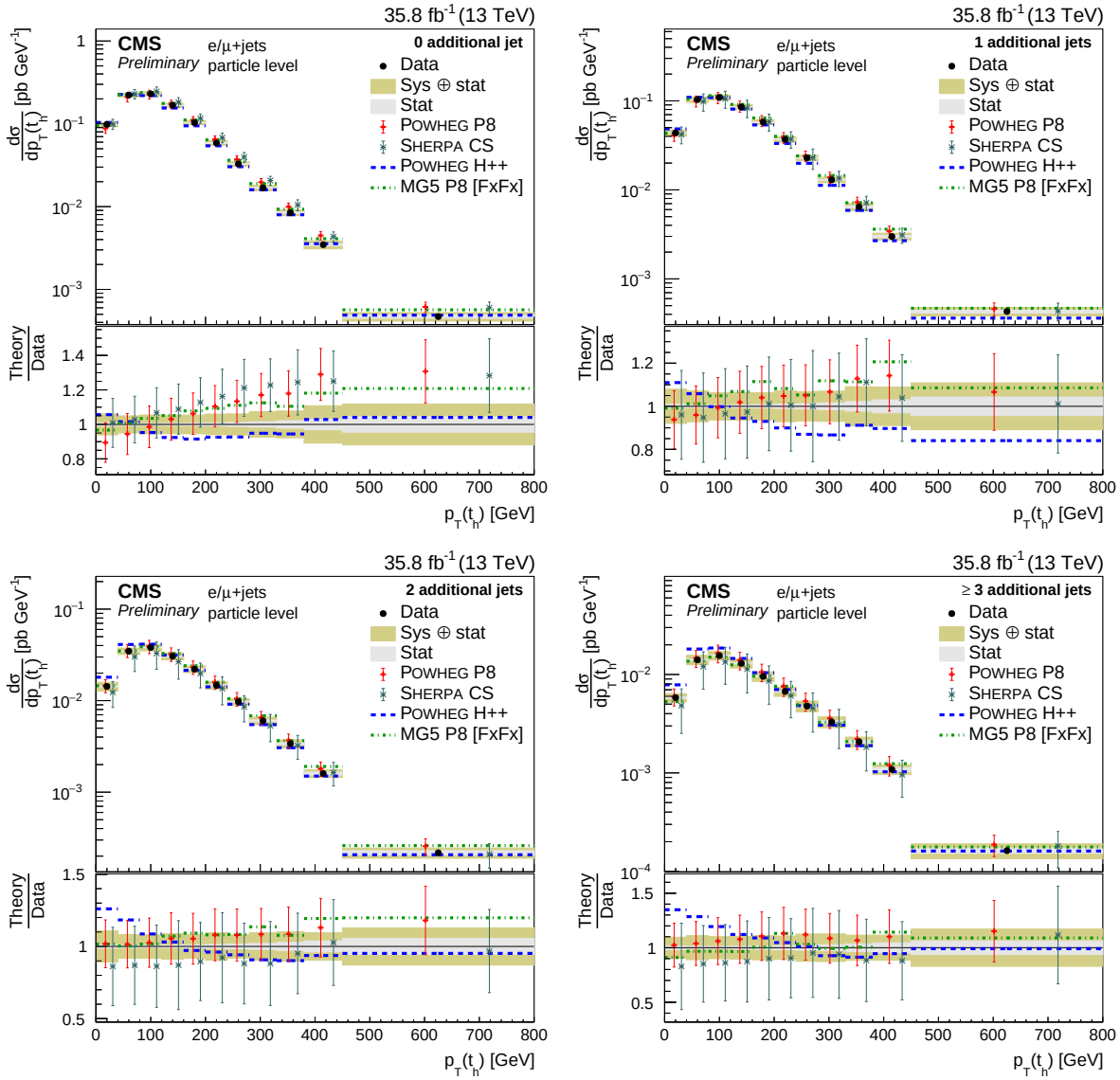

Figure 21: Differential cross sections at particle level as a function of $p_{\mathrm{T}}(\mathrm{t_h})$ in bins of the number of additional jets. The data are shown as points with light (dark) error bands indicating the statistical (statistical and systematic) uncertainties. The cross sections are compared to the predictions of POWHEG combined with PYTHIA8 (P8) or HERWIG++ (H++) and the multiparton simulations MG5_aMC@NLO (MG5)+PYTHIA8 FxFx and SHERPA. The ratios of the predictions to the measured cross sections are shown at the bottom of each panel.

atic uncertainties we assume a full correlation among all bins, while the various sources are assumed to be uncorrelated. The same assumptions about correlations are made for the theoretical uncertainties in the POWHEG+PYTHIA8 and the SHERPA predictions. In addition, we perform the χ^2 tests without any uncertainties in the theoretical models to compare the agreements with the central predictions. From the χ^2 values and the numbers of degrees of freedom, which corresponds to the number of bins in the distributions, the p-values are calculated. The results are shown in Table 1 for the parton-level and in Table 2 for the particle-level measurements.

Table 1: Comparison between the measured distributions at parton level and the predictions of POWHEG combined with PYTHIA8 (P8) or HERWIG++ (H++), the multiparton simulation MG5_aMC@NLO FxFx, and the NNLO QCD+NLO EW calculations. The compatibility with the POWHEG+PYTHIA8 prediction is also calculated under consideration of its theoretical uncertainties (with unc.), while those are not taken into account for the other comparisons. The results of the χ^2 tests are listed together with the numbers of degrees of freedom (dof) and the corresponding p-values.

Distribution	χ^2/dof	p-value	χ^2/dof	p-value	χ^2/dof	p-value
	POWHEG+P8 with unc.		POWHEG+P8		NNLO QCD+NLO EW	
$p_T(t_{high})$	16.4/12	0.173	27.4/12	< 0.01	36.9/12	< 0.01
$p_T(t_{low})$	22.4/12	0.033	42.7/12	< 0.01	77.2/12	< 0.01
$p_T(t_h)$	16.4/12	0.175	24.0/12	0.020	5.13/12	0.953
$\lvert y(t_h)\rvert$	1.28/11	1.000	1.41/11	1.000	2.27/11	0.997
$p_T(t_\ell)$	22.2/12	0.035	38.3/12	< 0.01	9.56/12	0.654
$\lvert y(t_\ell)\rvert$	2.04/11	0.998	2.42/11	0.996	8.14/11	0.700
$M(t\bar{t})$	7.67/10	0.661	11.6/10	0.314	24.7/10	< 0.01
$\lvert y(t\bar{t})\rvert$	3.98/10	0.948	5.66/10	0.843	9.26/10	0.507
$p_T(t\bar{t})$	5.38/8	0.717	46.5/8	< 0.01		
$\lvert y(t_h)\rvert$ *vs.* $p_T(t_h)$	23.6/44	0.995	41.6/44	0.577		
$M(t\bar{t})$ *vs.* $\lvert y(t\bar{t})\rvert$	20.6/35	0.975	35.0/35	0.469		
$M(t\bar{t})$ *vs.* Δy	24.9/40	0.971	35.1/40	0.689		
$p_T(t_h)$ *vs.* $M(t\bar{t})$	38.9/32	0.188	59.3/32	< 0.01		
	POWHEG+H++		MG5_aMC@NLO+P8 FxFx		—	
$p_T(t_{high})$	6.60/12	0.883	16.3/12	0.180		
$p_T(t_{low})$	28.5/12	< 0.01	15.3/12	0.225		
$p_T(t_h)$	5.09/12	0.955	11.0/12	0.530		
$\lvert y(t_h)\rvert$	2.39/11	0.997	2.21/11	0.998		
$p_T(t_\ell)$	6.55/12	0.886	17.4/12	0.136		
$\lvert y(t_\ell)\rvert$	2.54/11	0.995	3.99/11	0.970		
$M(t\bar{t})$	4.16/10	0.940	12.1/10	0.275		
$\lvert y(t\bar{t})\rvert$	11.9/10	0.292	8.92/10	0.540		
$p_T(t\bar{t})$	55.0/8	< 0.01	26.8/8	< 0.01		
$\lvert y(t_h)\rvert$ *vs.* $p_T(t_h)$	57.9/44	0.077	40.2/44	0.634		
$M(t\bar{t})$ *vs.* $\lvert y(t\bar{t})\rvert$	40.8/35	0.229	58.7/35	< 0.01		
$p_T(t_h)$ *vs.* $M(t\bar{t})$	93.0/32	< 0.01	166/32	< 0.01		

The χ^2 tests show that the measurements are compatible with the POWHEG+PYTHIA8 and SHERPA predictions if their uncertainties are taken into account. With the selected settings

Table 2: Comparison between the measured distributions at particle level and the predictions of POWHEG combined with PYTHIA8 (P8) or HERWIG++ (H++) and the multiparton simulations of MG5_aMC@NLO FxFx and SHERPA. The compatibilities with the POWHEG+PYTHIA8 and the SHERPA predictions are also calculated under consideration of their theoretical uncertainties (with unc.), while those are not taken into account for the other comparisons. The results of the χ^2 tests are listed together with the numbers of degrees of freedom (dof) and the corresponding p-values.

Distribution	χ^2/dof	p-value	χ^2/dof	p-value	χ^2/dof	p-value
	POWHEG+P8 with unc.		SHERPA with unc.		POWHEG+P8	
$p_{\mathrm{T}}(\mathrm{t_h})$	15.9/12	0.197	7.21/12	0.844	29.5/12	< 0.01
$\lvert y(\mathrm{t_h})\rvert$	1.96/11	0.999	1.48/11	1.000	2.23/11	0.997
$p_{\mathrm{T}}(\mathrm{t}_\ell)$	27.0/12	< 0.01	22.3/12	0.034	80.2/12	< 0.01
$\lvert y(\mathrm{t}_\ell)\rvert$	4.55/11	0.951	5.07/11	0.928	4.99/11	0.932
$M(\mathrm{t\bar{t}})$	5.83/10	0.829	2.40/10	0.992	9.07/10	0.525
$p_{\mathrm{T}}(\mathrm{t\bar{t}})$	4.96/8	0.761	28.9/8	< 0.01	41.2/8	< 0.01
$\lvert y(\mathrm{t\bar{t}})\rvert$	5.93/10	0.821	6.63/10	0.760	8.61/10	0.570
$\lvert y(\mathrm{t_h})\rvert$ *vs.* $p_{\mathrm{T}}(\mathrm{t_h})$	35.7/44	0.810	29.6/44	0.953	64.1/44	0.025
$M(\mathrm{t\bar{t}})$ *vs.* $\lvert y(\mathrm{t\bar{t}})\rvert$	25.9/35	0.867	24.2/35	0.914	56.2/35	0.013
$p_{\mathrm{T}}(\mathrm{t_h})$ *vs.* $M(\mathrm{t\bar{t}})$	47.4/32	0.039	57.2/32	< 0.01	73.2/32	< 0.01
	SHERPA		POWHEG+H++		MG5_aMC@NLO+P8 FxFx	
$p_{\mathrm{T}}(\mathrm{t_h})$	13.5/12	0.335	32.1/12	< 0.01	17.4/12	0.137
$\lvert y(\mathrm{t_h})\rvert$	2.32/11	0.997	4.89/11	0.936	3.16/11	0.988
$p_{\mathrm{T}}(\mathrm{t}_\ell)$	39.4/12	< 0.01	21.8/12	0.040	47.7/12	< 0.01
$\lvert y(\mathrm{t}_\ell)\rvert$	5.54/11	0.902	4.04/11	0.969	7.22/11	0.781
$M(\mathrm{t\bar{t}})$	2.86/10	0.985	52.8/10	< 0.01	5.45/10	0.859
$p_{\mathrm{T}}(\mathrm{t\bar{t}})$	68.7/8	< 0.01	46.8/8	< 0.01	21.3/8	< 0.01
$\lvert y(\mathrm{t\bar{t}})\rvert$	12.1/10	0.276	18.6/10	0.046	8.13/10	0.616
$\lvert y(\mathrm{t_h})\rvert$ *vs.* $p_{\mathrm{T}}(\mathrm{t_h})$	48.3/44	0.305	116/44	< 0.01	44.9/44	0.434
$M(\mathrm{t\bar{t}})$ *vs.* $\lvert y(\mathrm{t\bar{t}})\rvert$	41.5/35	0.208	219/35	< 0.01	55.7/35	0.014
$p_{\mathrm{T}}(\mathrm{t_h})$ *vs.* $M(\mathrm{t\bar{t}})$	66.5/32	< 0.01	152/32	< 0.01	48.9/32	0.028

SHERPA fails to describe $p_{\mathrm{T}}(\mathrm{t\bar{t}})$. In general, some tension is observed for the distributions of $p_{\mathrm{T}}(\mathrm{t})$. The NNLO QCD+NLO EW calculation of $p_{\mathrm{T}}(\mathrm{t})$ shows an improved agreement with the measurement compared to most of the NLO simulations. However, looking at $p_{\mathrm{T}}(\mathrm{t_{high}})$ and $p_{\mathrm{T}}(\mathrm{t_{low}})$ separately, we observe that the former is very well modeled, while the later is predicted to be harder. The comparisons to the various central prediction at parton and particle level shows that the multiparton simulation MG5_aMC@NLO+PYTHIA8 FxFx performs best.

11 Measurements of multiplicities and kinematic properties of jets

In the following we discuss the measurements involving multiplicities and kinematic properties of jets. These are performed at particle level only. In the POWHEG simulations all jets beyond one additional jet are only described by the parton-shower simulation and, hence, their description is subject to parton-shower tuning. In the SHERPA simulation the production of up to one additional jet is calculated at NLO, up to four jets are calculated at LO accuracy. However, these LO calculations are very sensitive to the choice of the scales. Since in the MG5_aMC@NLO+PYTHIA8 FxFx simulation up to two additional jets are calculated at NLO, it is expected to make the most accurate prediction at high jet multiplicities.

The differential cross sections as a function of $p_{\mathrm{T}}(\mathrm{t_h})$, $M(\mathrm{t\bar{t}})$, and $p_{\mathrm{T}}(\mathrm{t\bar{t}})$ in bins of the number of additional jets are shown in Figs. 21–23. These distributions are helpful to estimate the $\mathrm{t\bar{t}}$ background contribution in searches for physics beyond the standard model that are looking into signatures with high jet multiplicities.

Furthermore, we measure properties of individual jets. The differential cross sections as a function of p_{T} of jets in the $\mathrm{t\bar{t}}$ system and of the four leading additional jets are shown in Fig. 24. The trend of a softer p_{T} spectrum of the top quark compared to the PYTHIA8 simulations is also visible for all jets of the $\mathrm{t\bar{t}}$ system. These p_{T} distributions allow for the calculation of jet multiplicities with minimum p_{T} thresholds of 30, 50, 75, and 100 GeV and gap fractions [10, 12] shown in Fig. 25 and Fig. 26, respectively. The gap fraction $f_n(p_{\mathrm{T}})$ is the fraction of unfolded events that do not contain at least n additional jets above the given p_{T} threshold. In the calculations of jet multiplicities and gap fractions we take into account the small fraction of jets above the displayed p_{T} ranges. The uncertainties are obtained by error propagation under consideration of the full covariance matrices. The POWHEG+HERWIG++ prediction overestimates the jet multiplicity at low jet p_{T}, while POWHEG+PYTHIA8 predicts too many jets with high p_{T}.

In Figs. 27–29 the distributions of $|\eta|$, $\Delta R_{\mathrm{j_t}}$, and ΔR_{t} are shown. The differential cross section as a function of $|\eta|$ is well described by all simulations, while POWHEG+HERWIG++ overestimates the radiation of additional jets close to the jets in the $\mathrm{t\bar{t}}$ system. In the predictions such collinear radiation is mainly described of the parton-shower model.

In Table 3 the results of the χ^2 tests comparing the measurements involving multiplicities and kinematic properties of jets to the simulations are presented. The kinematic distributions and multiplicities of the additional jets are reasonably modeled by POWHEG+PYTHIA8, while with the selected settings SHERPA fails to describe them. The POWHEG descriptions of additional jets rely on phenomenological models of parton showering and hadronization and are quite different for PYTHIA8 and HERWIG++. At high jet multiplicities the LO SHERPA predictions strongly depends on the choice of scales. As expected, the multiparton simulation MG5_aMC@NLO+PYTHIA8 FxFx performs slightly better than the others.

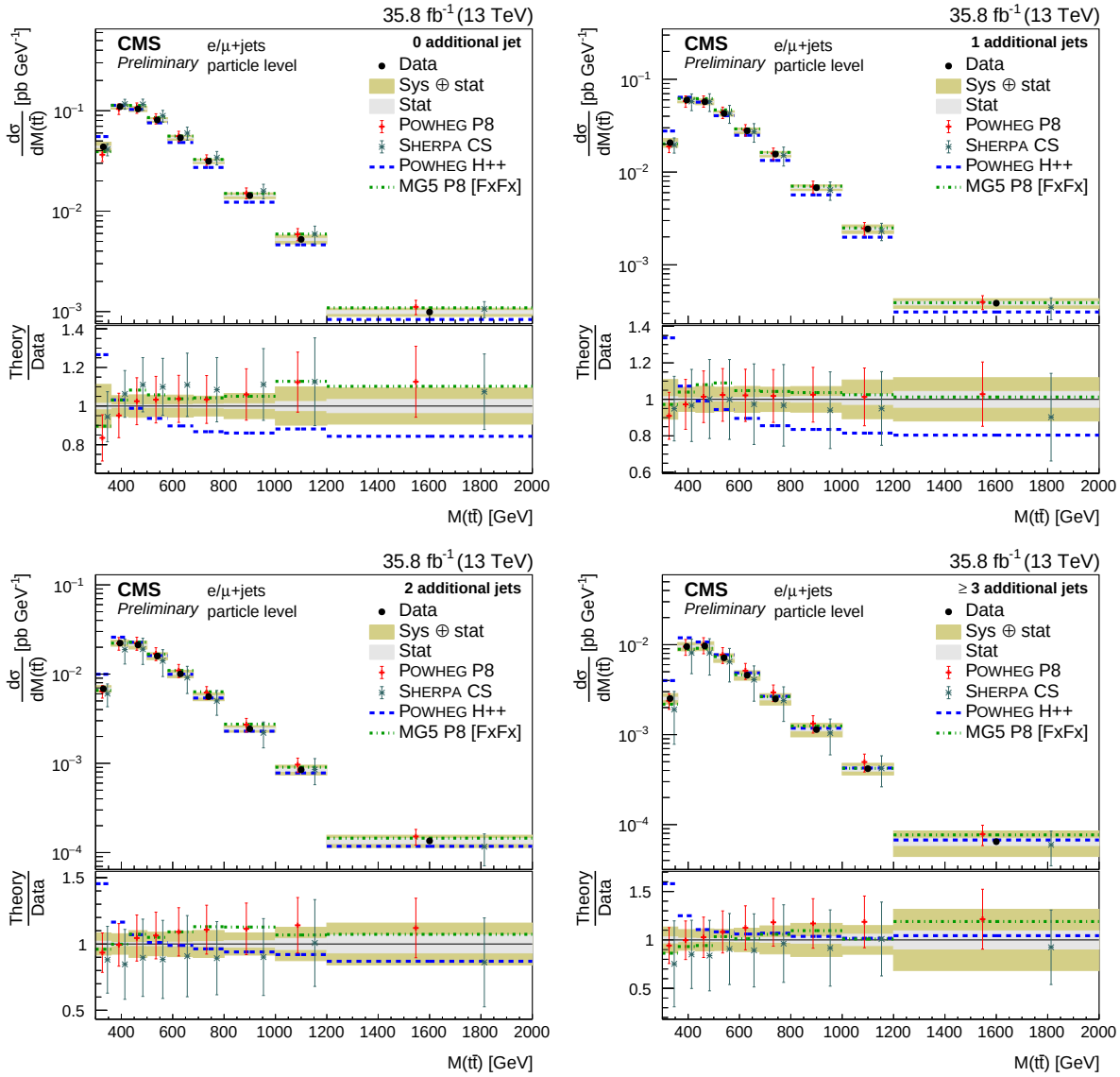

Figure 22: Differential cross sections at particle level as a function of $M(\mathrm{t\bar{t}})$ in bins of the number of additional jets. The data are shown as points with light (dark) error bands indicating the statistical (statistical and systematic) uncertainties. The cross sections are compared to the predictions of POWHEG combined with PYTHIA8 (P8) or HERWIG++ (H++) and the multiparton simulations MG5_aMC@NLO (MG5)+PYTHIA8 FxFx and SHERPA. The ratios of the predictions to the measured cross sections are shown at the bottom of each panel.

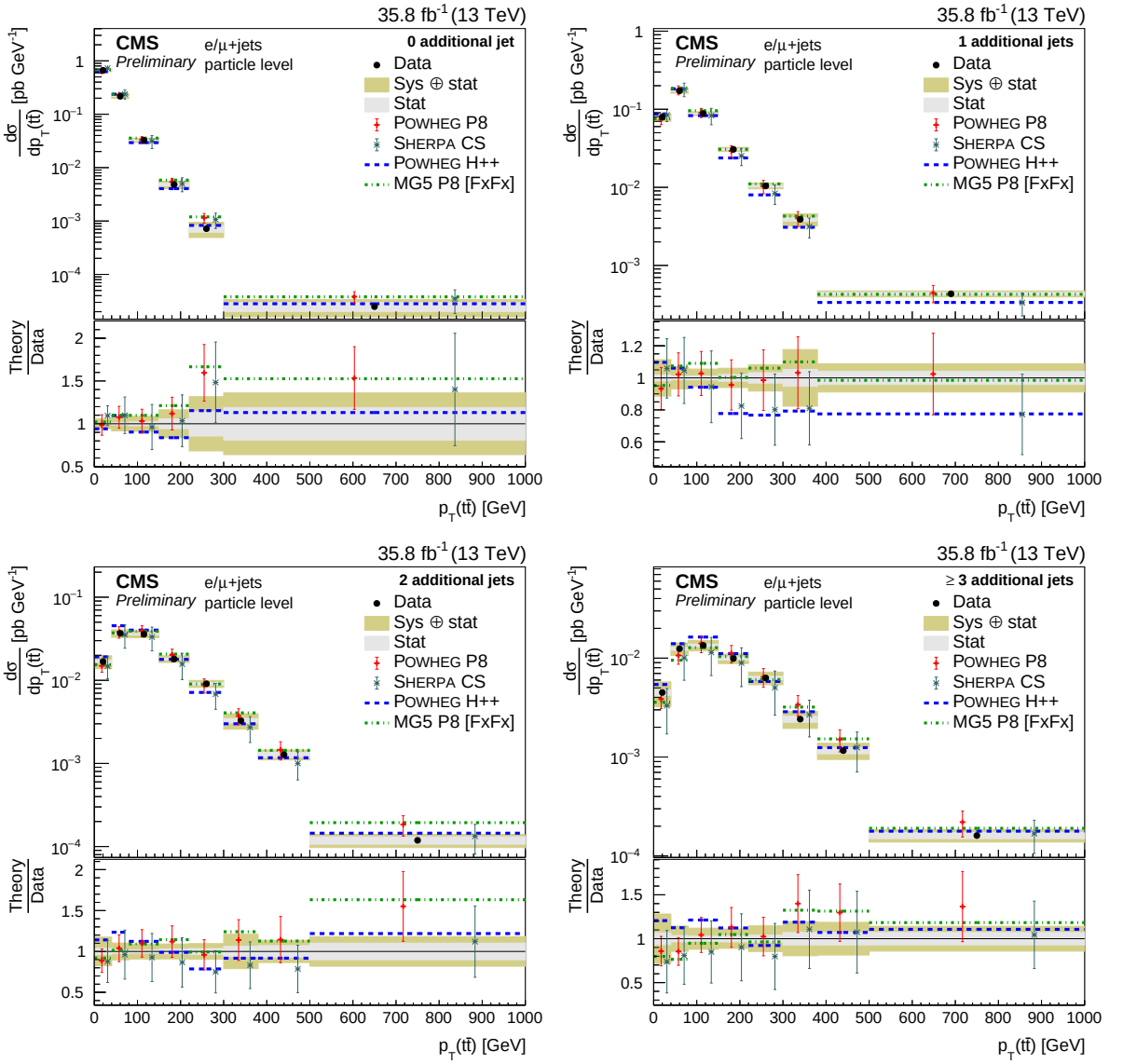

Figure 23: Differential cross sections at particle level as a function of $p_{\mathrm{T}}(\mathrm{t\bar{t}})$ in bins of the number of additional jets. The data are shown as points with light (dark) error bands indicating the statistical (statistical and systematic) uncertainties. The cross sections are compared to the predictions of POWHEG combined with PYTHIA8 (P8) or HERWIG++ (H++) and the multiparton simulations MG5_aMC@NLO (MG5)+PYTHIA8 FxFx and SHERPA. The ratios of the predictions to the measured cross sections are shown at the bottom of each panel.

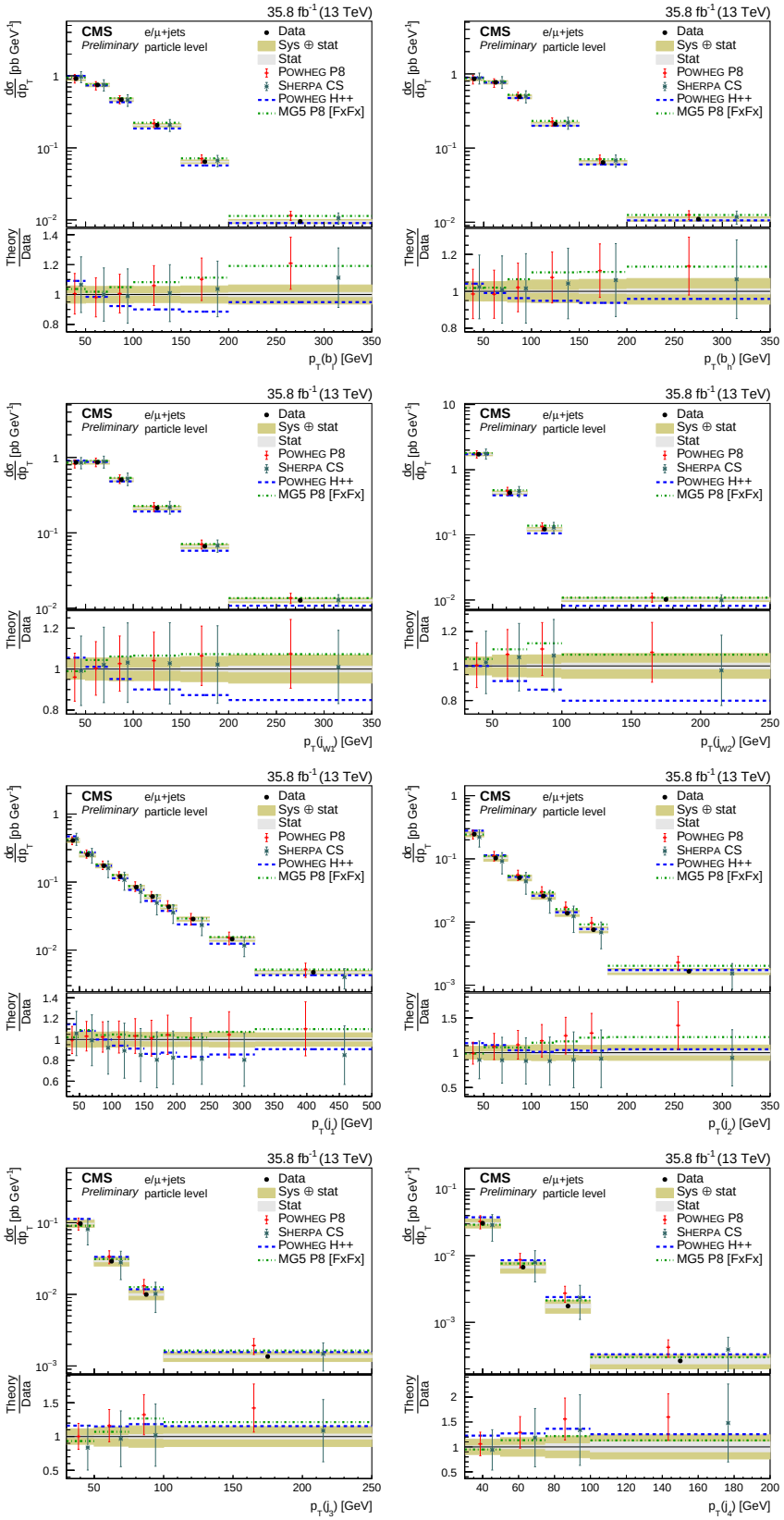

Figure 24: Differential cross section at particle level as a function of jet p_{T}. The data are shown as points with light (dark) error bands indicating the statistical (statistical and systematic) uncertainties. The cross sections are compared to the predictions of POWHEG combined with PYTHIA8 (P8) or HERWIG++ (H++) and the multiparton simulations MG5_aMC@NLO (MG5)+PYTHIA8 FxFx and SHERPA. The ratios of the predictions to the measured cross sections are shown at the bottom of each panel.

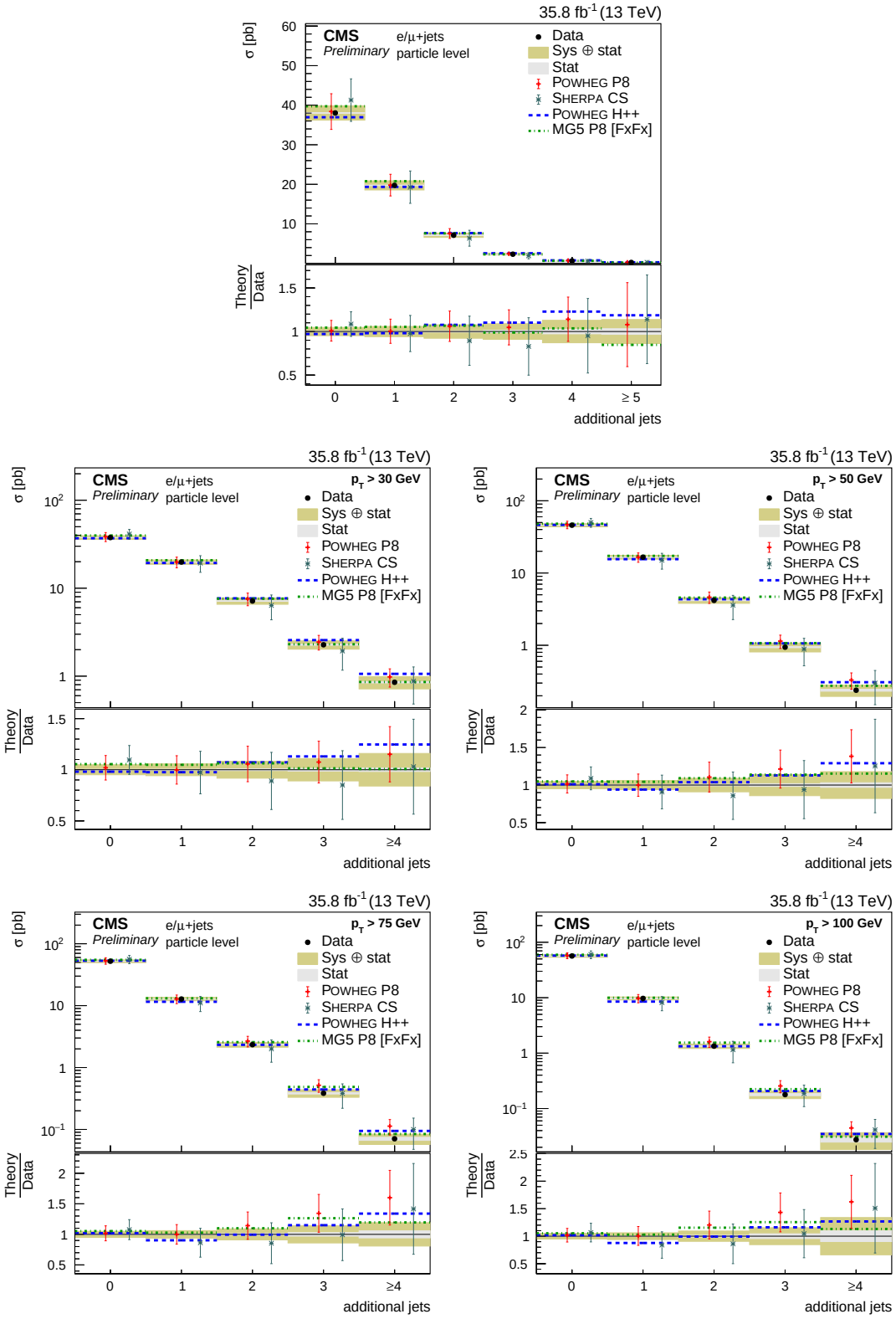

Figure 25: Top: jet multiplicity. Middle, Bottom: jet multiplicities for various thresholds of the jet p_{T}. The data are shown as points with light (dark) error bands indicating the statistical (statistical and systematic) uncertainties. The cross sections are compared to the predictions of POWHEG combined with PYTHIA8 (P8) or HERWIG++ (H++) and the multiparton simulations MG5_aMC@NLO (MG5)+PYTHIA8 FxFx and SHERPA. The ratios of the predictions to the measured cross sections are shown at the bottom of each panel.

Table 3: Comparison between the measurements involving multiplicities and kinematic properties of jets and the predictions of POWHEG combined with PYTHIA8 (P8) or HERWIG++ (H++) and the multiparton simulations of MG5_aMC@NLO FxFx and SHERPA. The compatibilities with the POWHEG+PYTHIA8 and the SHERPA predictions are also calculated under consideration of their theoretical uncertainties (with unc.), while those are not taken into account for the other comparisons. The results of the χ^2 tests are listed together with the numbers of degrees of freedom (dof) and the corresponding p-values.

Distribution	χ^2/dof	p-value	χ^2/dof	p-value	χ^2/dof	p-value
	POWHEG+P8 with unc.		SHERPA with unc.		POWHEG+P8	
Additional jets	1.52/6	0.958	27.3/6	< 0.01	10.1/6	0.121
Additional jets *vs.* $M(\mathrm{t\bar{t}})$	27.5/36	0.845	68.9/36	< 0.01	38.8/36	0.345
Additional jets *vs.* $p_{\mathrm{T}}(\mathrm{t_h})$	35.1/44	0.830	64.6/44	0.023	71.6/44	< 0.01
Additional jets *vs.* $p_{\mathrm{T}}(\mathrm{t\bar{t}})$	64.6/29	< 0.01	181/29	< 0.01	175/29	< 0.01
$p_{\mathrm{T}}(\mathrm{jet})$	70.2/47	0.016	374/47	< 0.01	133/47	< 0.01
$\lvert\eta(\mathrm{jet})\rvert$	120/70	< 0.01	174/70	< 0.01	171/70	< 0.01
$\Delta R_{\mathrm{j_t}}$	60.9/66	0.655	215/66	< 0.01	168/66	< 0.01
ΔR_{t}	64.0/62	0.405	229/62	< 0.01	121/62	< 0.01
	SHERPA		POWHEG+H++		MG5_aMC@NLO+P8 FxFx	
Additional jets	63.0/6	< 0.01	34.1/6	< 0.01	11.1/6	0.086
Additional jets *vs.* $M(\mathrm{t\bar{t}})$	112/36	< 0.01	300/36	< 0.01	55.1/36	0.022
Additional jets *vs.* $p_{\mathrm{T}}(\mathrm{t_h})$	88.5/44	< 0.01	230/44	< 0.01	53.4/44	0.156
Additional jets *vs.* $p_{\mathrm{T}}(\mathrm{t\bar{t}})$	285/29	< 0.01	223/29	< 0.01	122/29	< 0.01
$p_{\mathrm{T}}(\mathrm{jet})$	768/47	< 0.01	624/47	< 0.01	111/47	< 0.01
$\lvert\eta(\mathrm{jet})\rvert$	214/70	< 0.01	259/70	< 0.01	133/70	< 0.01
$\Delta R_{\mathrm{j_t}}$	334/66	< 0.01	959/66	< 0.01	67.0/66	0.441
ΔR_{t}	316/62	< 0.01	483/62	< 0.01	78.9/62	0.073

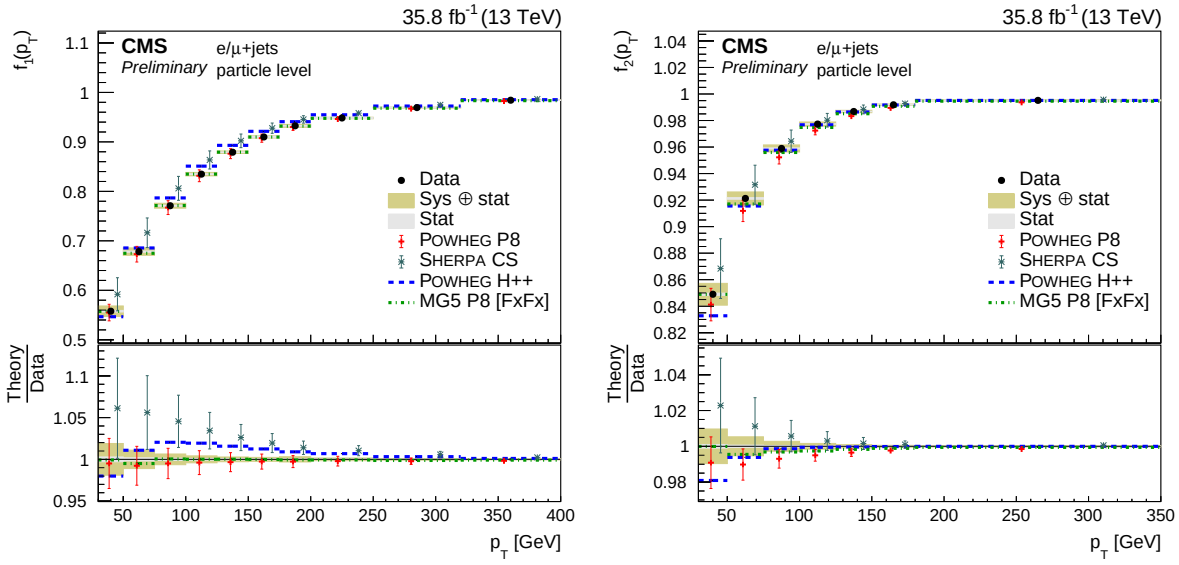

Figure 26: Distributions of $f_1(p_T)$ and $f_2(p_T)$. The data are shown as points with light (dark) error bands indicating the statistical (statistical and systematic) uncertainties. The measurements are compared to the predictions of POWHEG combined with PYTHIA8 (P8) or HERWIG++ (H++) and the multiparton simulations MG5_aMC@NLO (MG5)+PYTHIA8 FxFx and SHERPA. The ratios of the predictions to the measured cross sections are shown at the bottom of each panel.

12 Summary

Measurements of the differential and double-differential cross sections for $t\bar{t}$ production in pp collisions at 13 TeV have been presented. The data correspond to an integrated luminosity of 35.8 fb^{-1} recorded by the CMS experiment. The $t\bar{t}$ production cross section is measured in the ℓ+jets channels at particle and parton level channel as a function of transverse momentum p_T and rapidity $|y|$ of the top quarks; p_T, $|y|$, and invariant mass of the $t\bar{t}$ system. In addition, at particle level detailed studies of multiplicities and kinematic properties of the jets in $t\bar{t}$ events have been performed. The dominant sources of uncertainty are the jet energy scale uncertainties on the experimental side and parton shower modeling on the theoretical side.

The results are compared to several standard model predictions that use different methods and approximations for their calculations. The kinematic properties of the top quarks and the $t\bar{t}$ system are well described apart from a softer measured p_T of the top quarks, which has already been observed in previous measurements and can partially be explained by calculations including NNLO QCD and NLO EW corrections. The kinematic distributions and multiplicities of the additional jets are reasonably modeled by POWHEG+PYTHIA8. However, the POWHEG descriptions of additional jets rely on phenomenological models of parton showering and hadronization with tuned parameters. With the selected settings the SHERPA predictions show larger discrepancies from the data, but they strongly depend on the choice of scales. The multiparton simulation of MG5_aMC@NLO+PYTHIA8 FxFx results in the best agreement with the measurements.

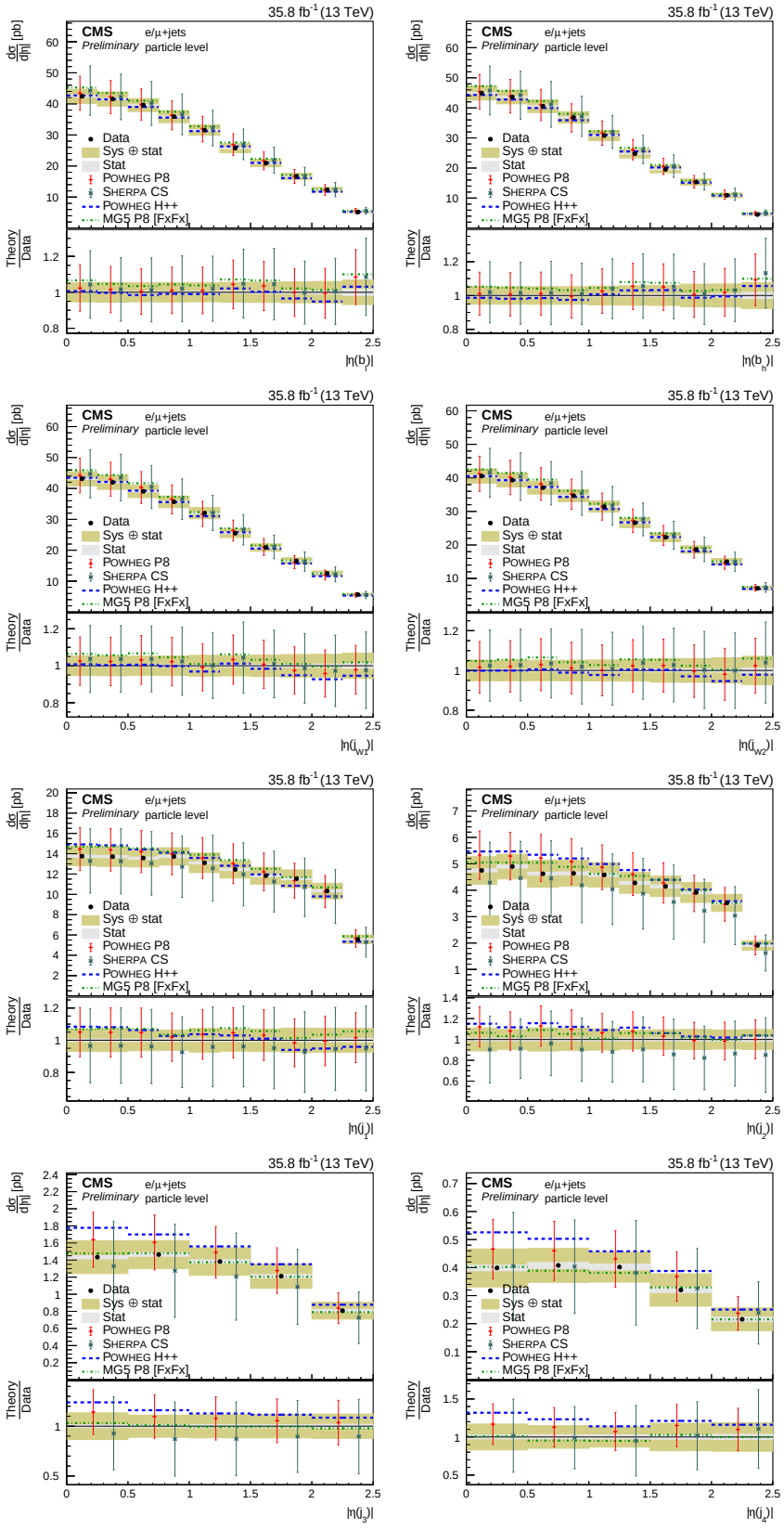

Figure 27: Differential cross section at particle level as a function of jet η. The data are shown as points with light (dark) error bands indicating the statistical (statistical and systematic) uncertainties. The cross sections are compared to the predictions of POWHEG combined with PYTHIA8 (P8) or HERWIG++ (H++) and the multiparton simulations MG5_aMC@NLO (MG5)+PYTHIA8 FxFx and SHERPA. The ratios of the predictions to the measured cross sections are shown at the bottom of each panel.

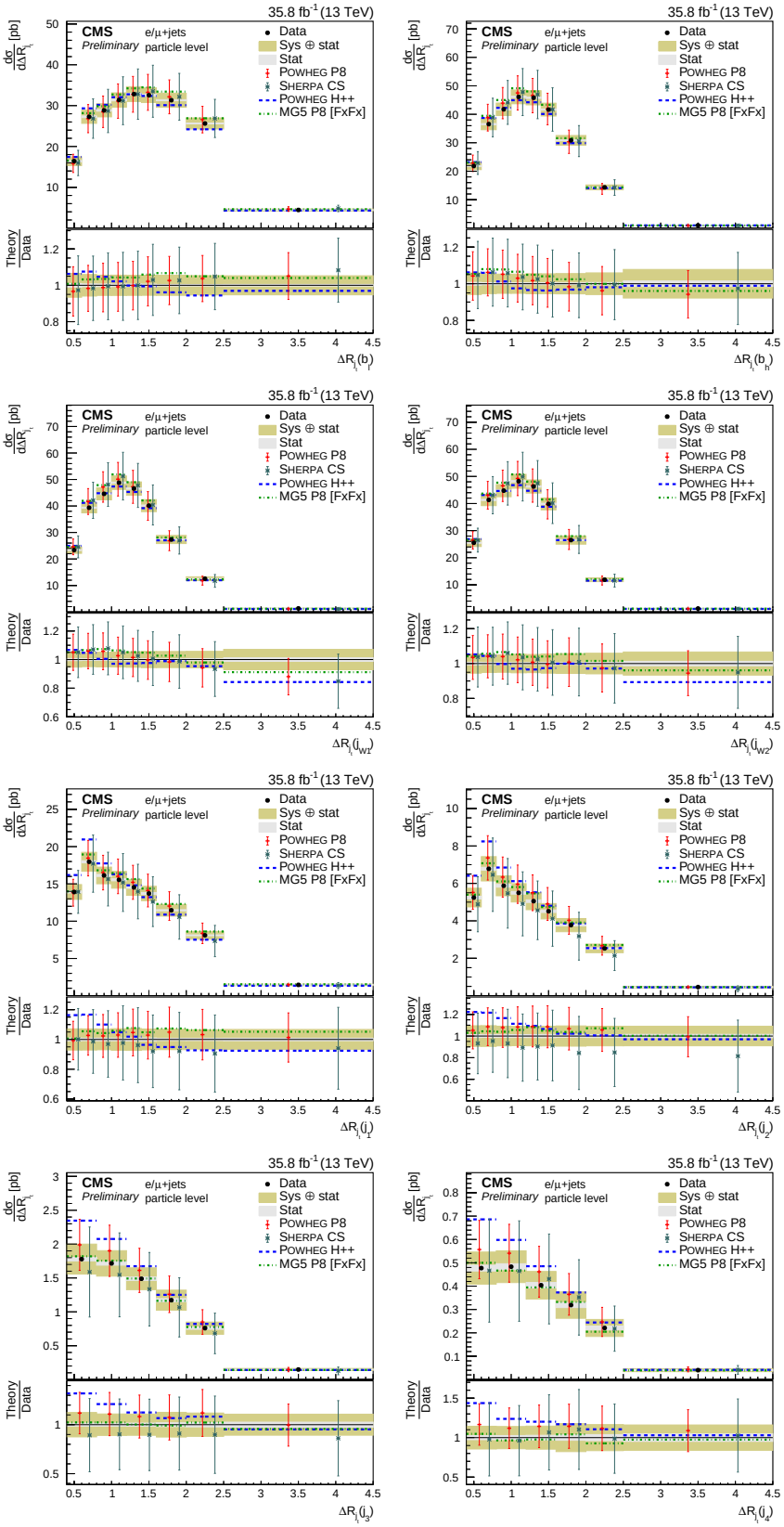

Figure 28: Differential cross section at particle level as a function of jet ΔR_{jt}. The data are shown as points with light (dark) error bands indicating the statistical (statistical and systematic) uncertainties. The cross sections are compared to the predictions of POWHEG combined with PYTHIA8 (P8) or HERWIG++ (H++) and the multiparton simulations MG5_aMC@NLO (MG5)+PYTHIA8 FxFx and SHERPA. The ratios of the predictions to the measured cross sections are shown at the bottom of each panel.

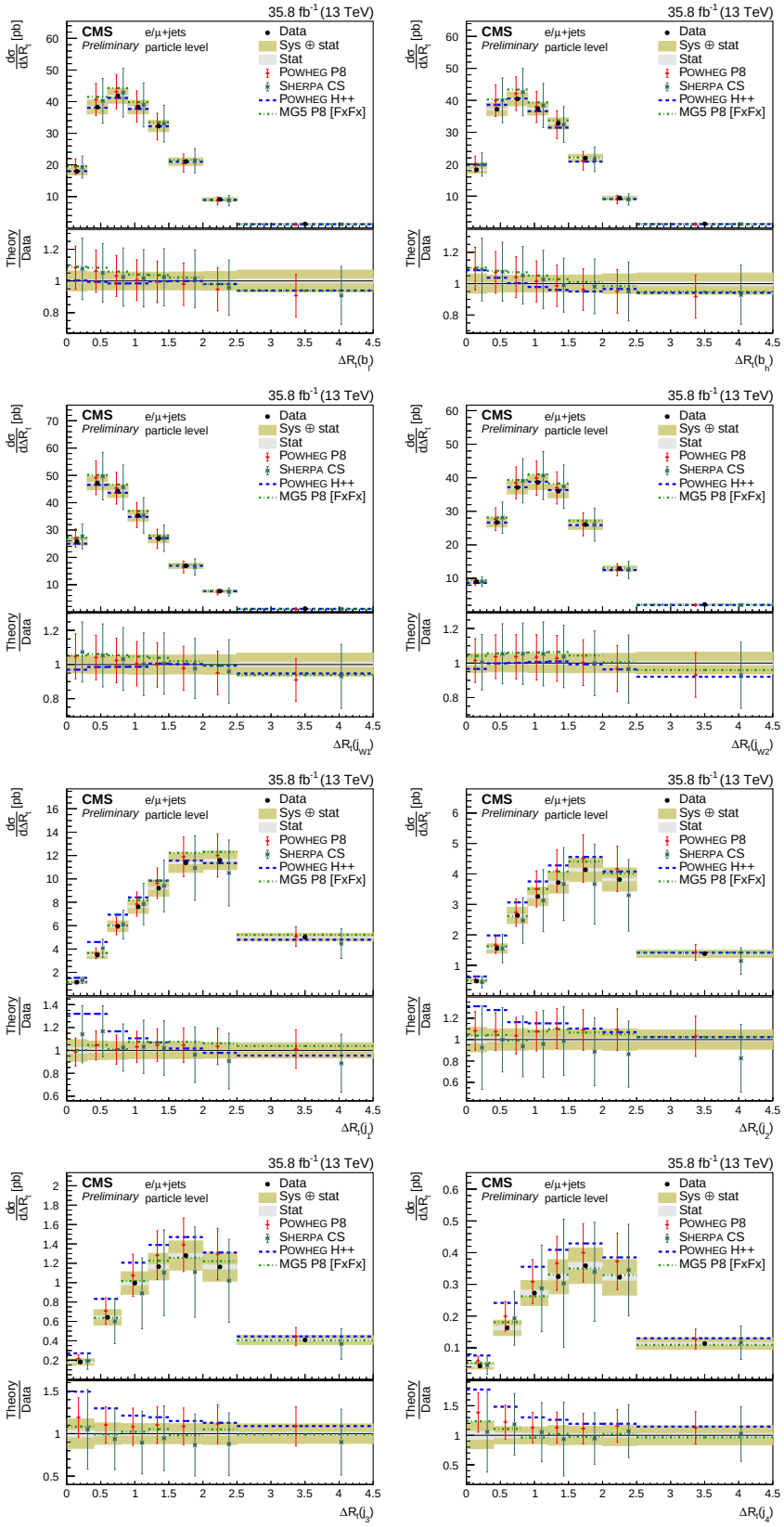

Figure 29: Differential cross section at particle level as a function of ΔR_t. The data are shown as points with light (dark) error bands indicating the statistical (statistical and systematic) uncertainties. The cross sections are compared to the predictions of POWHEG combined with PYTHIA8 (P8) or HERWIG++ (H++) and the multiparton simulations MG5_aMC@NLO (MG5)+PYTHIA8 FxFx and SHERPA. The ratios of the predictions to the measured cross sections are shown at the bottom of each panel.

References

[1] CMS Collaboration, "Cms luminosity measurement for the 2016 data taking period", CMS Physics Analysis Summary CMS-PAS-LUM-17-001, 2017.

[2] CMS Collaboration, "Measurement of differential top-quark pair production cross sections in pp colisions at $\sqrt{s} = 7$ TeV", *Eur. Phys. J. C* **73** (2013) 2339, doi:10.1140/epjc/s10052-013-2339-4, arXiv:1211.2220.

[3] ATLAS Collaboration, "Differential top-antitop cross-section measurements as a function of observables constructed from final-state particles using pp collisions at $\sqrt{s} = 7$ TeV in the ATLAS detector", *JHEP* **06** (2015) 100, doi:10.1007/JHEP06(2015)100, arXiv:1502.05923.

[4] CMS Collaboration, "Measurement of the differential cross section for top quark pair production in pp collisions at $\sqrt{s} = 8$ TeV", *Eur. Phys. J. C* **75** (2015) 542, doi:10.1140/epjc/s10052-015-3709-x, arXiv:1505.04480.

[5] ATLAS Collaboration, "Measurements of top-quark pair differential cross-sections in the lepton+jets channel in pp collisions at $\sqrt{s} = 8$ TeV using the ATLAS detector", *Eur. Phys. J. C* **76** (2016) 538, doi:10.1140/epjc/s10052-016-4366-4, arXiv:1511.04716.

[6] ATLAS Collaboration, "Measurement of the differential cross-section of highly boosted top quarks as a function of their transverse momentum in $\sqrt{s}$ = 8 TeV proton-proton collisions using the ATLAS detector", *Phys. Rev. D* **93** (2016) 032009, doi:10.1103/PhysRevD.93.032009, arXiv:1510.03818.

[7] CMS Collaboration, "Measurement of the $\mathrm{t\bar{t}}$ production cross section in the all-jets final state in pp collisions at $\sqrt{s} = 8$ TeV", *Eur. Phys. J. C* **76** (2016) 128, doi:10.1140/epjc/s10052-016-3956-5, arXiv:1509.06076.

[8] CMS Collaboration, "Measurement of the integrated and differential $\mathrm{t\bar{t}}$ production cross sections for high-p_{T} top quarks in pp collisions at $\sqrt{s} = 8$ TeV", *Phys. Rev. D* **94** (2016) 072002, doi:10.1103/PhysRevD.94.072002, arXiv:1605.00116.

[9] CMS Collaboration, "Measurement of the differential cross sections for top quark pair production as a function of kinematic event variables in pp collisions at $\sqrt{s}$=7 and 8 TeV", *Phys. Rev. D* **94** (2016) 052006, doi:10.1103/PhysRevD.94.052006, arXiv:1607.00837.

[10] CMS Collaboration, "Measurement of $\mathrm{t\bar{t}}$ production with additional jet activity, including b quark jets, in the dilepton decay channel using pp collisions at $\sqrt{s} = 8$ TeV", *Eur. Phys. J. C* **76** (2016) 379, doi:10.1140/epjc/s10052-016-4105-x, arXiv:1510.03072.

[11] ATLAS Collaboration, "Measurement of top quark pair differential cross-sections in the dilepton channel in pp collisions at $\sqrt{s}$ = 7 and 8 TeV with ATLAS", *Phys. Rev. D* **94** (2016) 092003, doi:10.1103/PhysRevD.94.092003, arXiv:1607.07281.

[12] ATLAS Collaboration, "Measurement of jet activity in top quark events using the $e\mu$ final state with two b-tagged jets in pp collisions at $\sqrt{s} = 8$ TeV with the ATLAS detector", *JHEP* **09** (2016) 074, doi:10.1007/JHEP09(2016)074, arXiv:1606.09490.

[13] ATLAS Collaboration, "Measurement of jet activity produced in top-quark events with an electron, a muon and two b-tagged jets in the final state in pp collisions at

$\sqrt{s} = 13$ TeV with the ATLAS detector", *Eur. Phys. J. C* **77** (2017) 220, doi:10.1140/epjc/s10052-017-4766-0, arXiv:1610.09978.

[14] ATLAS Collaboration, "Measurements of top-quark pair differential cross-sections in the $e\mu$ channel in pp collisions at $\sqrt{s} = 13$ TeV using the ATLAS detector", *Eur. Phys. J. C* **77** (2017) 292, doi:10.1140/epjc/s10052-017-4821-x, arXiv:1612.05220.

[15] CMS Collaboration, "Measurement of differential cross sections for top quark pair production using the lepton+jets final state in proton-proton collisions at 13 TeV", *Phys. Rev. D* **95** (2017) 092001, doi:10.1103/PhysRevD.95.092001, arXiv:1610.04191.

[16] P. Nason, "A new method for combining NLO QCD with shower Monte Carlo algorithms", *JHEP* **11** (2004) 040, doi:10.1088/1126-6708/2004/11/040, arXiv:hep-ph/0409146.

[17] S. Frixione, P. Nason, and C. Oleari, "Matching NLO QCD computations with Parton Shower simulations: the POWHEG method", *JHEP* **11** (2007) 070, doi:10.1088/1126-6708/2007/11/070, arXiv:0709.2092.

[18] S. Alioli, P. Nason, C. Oleari, and E. Re, "A general framework for implementing NLO calculations in shower Monte Carlo programs: the POWHEG BOX", *JHEP* **06** (2010) 043, doi:10.1007/JHEP06(2010)043, arXiv:1002.2581.

[19] J. M. Campbell, R. K. Ellis, P. Nason, and E. Re, "Top-pair production and decay at NLO matched with parton showers", *JHEP* **04** (2015) 114, doi:10.1007/JHEP04(2015)114, arXiv:1412.1828.

[20] J. Alwall et al., "The automated computation of tree-level and next-to-leading order differential cross sections, and their matching to parton shower simulations", *JHEP* **07** (2014) 079, doi:10.1007/JHEP07(2014)079, arXiv:1405.0301.

[21] T. Sjöstrand, S. Mrenna, and P. Skands, "PYTHIA 6.4 physics and manual", *JHEP* **05** (2006) 026, doi:10.1088/1126-6708/2006/05/026, arXiv:hep-ph/0603175.

[22] T. Sjöstrand, S. Mrenna, and P. Z. Skands, "A brief introduction to PYTHIA 8.1", *Comput. Phys. Commun.* **178** (2008) 852, doi:10.1016/j.cpc.2008.01.036, arXiv:0710.3820.

[23] P. Skands, S. Carrazza, and J. Rojo, "Tuning PYTHIA 8.1: the Monash 2013 Tune", *Eur. Phys. J. C* **74** (2014) 3024, doi:10.1140/epjc/s10052-014-3024-y, arXiv:1404.5630.

[24] R. Frederix and S. Frixione, "Merging meets matching in MC@NLO", *JHEP* **12** (2012) 061, doi:10.1007/JHEP12(2012)061, arXiv:1209.6215.

[25] NNPDF Collaboration, "Parton distributions for the LHC Run II", *JHEP* **04** (2015) 040, doi:10.1007/JHEP04(2015)040, arXiv:1410.8849.

[26] M. Czakon and A. Mitov, "Top++: A Program for the Calculation of the Top-Pair Cross-Section at Hadron Colliders", *Comput. Phys. Commun.* **185** (2014) 2930, doi:10.1016/j.cpc.2014.06.021, arXiv:1112.5675.

[27] M. Bähr et al., "Herwig++ physics and manual", *Eur. Phys. J. C* **58** (2008) 639, doi:10.1140/epjc/s10052-008-0798-9, arXiv:0803.0883.

[28] M. H. Seymour and A. Siodmok, "Constraining MPI models using σ_{eff} and recent Tevatron and LHC Underlying Event data", *JHEP* **10** (2013) 113, doi:10.1007/JHEP10(2013)113, arXiv:1307.5015.

[29] E. Re, "Single-top Wt-channel production matched with parton showers using the POWHEG method", *Eur. Phys. J. C* **71** (2011) 1547, doi:10.1140/epjc/s10052-011-1547-z, arXiv:1009.2450.

[30] Y. Li and F. Petriello, "Combining QCD and electroweak corrections to dilepton production in FEWZ", *Phys. Rev. D* **86** (2012) 094034, doi:10.1103/PhysRevD.86.094034, arXiv:1208.5967.

[31] P. Kant et al., "HatHor for single top-quark production: Updated predictions and uncertainty estimates for single top-quark production in hadronic collisions", *Comput. Phys. Commun.* **191** (2015) 74, doi:10.1016/j.cpc.2015.02.001, arXiv:1406.4403.

[32] N. Kidonakis, "NNLL threshold resummation for top-pair and single-top production", *Phys. Part. Nucl.* **45** (2014) 714, doi:10.1134/S1063779614040091, arXiv:1210.7813.

[33] J. Allison et al., "Geant4 developments and applications", *IEEE Trans. Nucl. Sci.* **53** (2006) 270, doi:10.1109/TNS.2006.869826.

[34] CMS Collaboration, "Object definitions for top quark analyses at the particle level", CMS Note CERN-CMS-NOTE-2017-004, 2017.

[35] M. Cacciari, G. P. Salam, and G. Soyez, "The anti-k_t jet clustering algorithm", *JHEP* **04** (2008) 063, doi:10.1088/1126-6708/2008/04/063, arXiv:0802.1189.

[36] M. Cacciari, G. P. Salam, and G. Soyez, "FastJet user manual", *Eur. Phys. J. C* **72** (2012) 1896, doi:10.1140/epjc/s10052-012-1896-2, arXiv:1111.6097.

[37] CMS Collaboration, "Performance of CMS muon reconstruction in pp collision events at $\sqrt{s} = 7$ TeV", *JINST* **7** (2012) P10002, doi:10.1088/1748-0221/7/10/P10002, arXiv:1206.4071.

[38] M. Cacciari and G. P. Salam, "Pileup subtraction using jet areas", *Phys. Lett. B* **659** (2008) 119, doi:10.1016/j.physletb.2007.09.077, arXiv:0707.1378.

[39] CMS Collaboration, "Performance of electron reconstruction and selection with the CMS detector in proton-proton collisions at $\sqrt{s} = 8$ TeV", *JINST* **10** (2015) P06005, doi:10.1088/1748-0221/10/06/P06005, arXiv:1502.02701.

[40] CMS Collaboration, "Jet energy scale and resolution in the CMS experiment in pp collisions at 8 TeV", *JINST* **12** (2017) P02014, doi:10.1088/1748-0221/12/02/P02014, arXiv:1607.03663.

[41] CMS Collaboration, "Identification of b quark jets at the CMS Experiment in the LHC Run 2", CMS Physics Analysis Summary CMS-PAS-BTV-15-001, 2016.

[42] B. A. Betchart, R. Demina, and A. Harel, "Analytic solutions for neutrino momenta in decay of top quarks", *Nucl. Instrum. Meth. A* **736** (2014) 169, doi:10.1016/j.nima.2013.10.039, arXiv:1305.1878.

[43] G. D'Agostini, "A multidimensional unfolding method based on Bayes' theorem", *Nucl. Instrum. Meth. A* **362** (1995) 487, doi:10.1016/0168-9002(95)00274-X.

[44] CMS Collaboration, "Investigations of the impact of the parton shower tuning in Pythia 8 in the modelling of $\mathrm{t\bar{t}}$ at $\sqrt{s} = 8$ and 13 TeV", CMS Physics Analysis Summary CMS-PAS-TOP-16-021, 2016.

[45] Particle Data Group Collaboration, "Review of Particle Physics", *Chin. Phys. C* **38** (2014) 090001, doi:10.1088/1674-1137/38/9/090001.

[46] M. Czakon et al., "Top-pair production at the LHC through NNLO QCD and NLO EW", (2017). arXiv:1705.04105.

[47] A. Manohar, P. Nason, G. P. Salam, and G. Zanderighi, "How bright is the proton? A precise determination of the photon parton distribution function", *Phys. Rev. Lett.* **117** (2016), no. 24, 242002, doi:10.1103/PhysRevLett.117.242002, arXiv:1607.04266.

[48] T. Gleisberg et al., "Event generation with SHERPA 1.1", *JHEP* **02** (2009) 007, doi:10.1088/1126-6708/2009/02/007, arXiv:0811.4622.

[49] F. Cascioli, P. Maierhöfer, and S. Pozzorini, "Scattering amplitudes with open loops", *Phys. Rev. Lett.* **108** (Mar, 2012) 111601, doi:10.1103/PhysRevLett.108.111601.

[50] S. Schumann and F. Krauss, "A Parton shower algorithm based on Catani-Seymour dipole factorisation", *JHEP* **03** (2008) 038, doi:10.1088/1126-6708/2008/03/038, arXiv:0709.1027.